



HAL
open science

Alcam-a and Pdgfr- α are essential for the development of sclerotome-derived stromal cells that support hematopoiesis

Emi Murayama, Catherine Vivier, Anne Schmidt, Philippe Herbomel

► **To cite this version:**

Emi Murayama, Catherine Vivier, Anne Schmidt, Philippe Herbomel. Alcam-a and Pdgfr- α are essential for the development of sclerotome-derived stromal cells that support hematopoiesis. Nature Communications, 2023, 14 (1), pp.1171. 10.1038/s41467-023-36612-y . hal-04233146v2

HAL Id: hal-04233146

<https://hal.science/hal-04233146v2>

Submitted on 16 Oct 2023

HAL is a multi-disciplinary open access archive for the deposit and dissemination of scientific research documents, whether they are published or not. The documents may come from teaching and research institutions in France or abroad, or from public or private research centers.

L'archive ouverte pluridisciplinaire **HAL**, est destinée au dépôt et à la diffusion de documents scientifiques de niveau recherche, publiés ou non, émanant des établissements d'enseignement et de recherche français ou étrangers, des laboratoires publics ou privés.



Distributed under a Creative Commons Attribution 4.0 International License

Alcam-a and Pdgfr- α are essential for the development of sclerotome-derived stromal cells that support hematopoiesis

Received: 27 February 2022

Accepted: 9 February 2023

Published online: 01 March 2023

 Check for updatesEmi Murayama ^{1,2,3} ✉, Catherine Vivier^{1,3}, Anne Schmidt ^{1,3} & Philippe Herbomel ^{1,3}

Mesenchymal stromal cells are essential components of hematopoietic stem and progenitor cell (HSPC) niches, regulating HSPC proliferation and fates. Their developmental origins are largely unknown. In zebrafish, we previously found that the stromal cells of the caudal hematopoietic tissue (CHT), a niche functionally homologous to the mammalian fetal liver, arise from the ventral part of caudal somites. We have now found that this ventral domain is the sclerotome, and that two markers of mammalian mesenchymal stem/stromal cells, Alcam and Pdgfr- α , are distinctively expressed there and instrumental for the emergence and migration of stromal cell progenitors, which in turn conditions the proper assembly of the vascular component of the CHT niche. Furthermore, we find that trunk somites are similarly dependent on Alcam and Pdgfr- α to produce mesenchymal cells that foster HSPC emergence from the aorta. Thus the sclerotome contributes essential stromal cells for each of the key steps of developmental hematopoiesis.

Hematopoietic stem and progenitor cells (HSPCs) are multipotent precursors that have the self-renewal capacity and continuously replenish all mature blood cells throughout the life span. In zebrafish as in mammalian development, they initially emerge from the dorsal aorta of the embryo through an endothelial hematopoietic transition (EHT)^{1–4}. Then they enter the bloodstream to reach their first niche, the caudal hematopoietic tissue (CHT)⁵, where they expand and undergo their first multi-lineage differentiation⁶. Thus the CHT in fish is the hematopoietic homolog of the fetal liver in mammals. In our previous work, we showed that the CHT niche was mainly composed of a transient venous plexus arising from the primitive caudal vein, and mesenchymal stromal cells interconnecting as well as lining the branches of this venous plexus^{5,7}—a structure basically similar to that of mammalian hematopoietic niches⁸.

We then discovered that the progenitors of these stromal cells initially arose from the ventral part of the caudal somites through an epithelial–mesenchymal transition (EMT)⁷. These stromal cell progenitors (SCPs) then emigrated further ventrally, in close interaction with the endothelial cells sprouting from the primitive caudal vein that

would make up the venous plexus, the other main component of the niche⁷. In the present study, we have further characterized the process of SCP emergence and emigration from the caudal somites and identified important molecular actors in this process.

The sclerotome compartment of somites, which has been more studied in the trunk, also lies at their ventromedial side and undergoes EMT and subsequent emigration, to produce axial cartilage and bone around the notochord^{9,10}, as well as other derivatives such as mural cells around blood vessels^{11–14} and tendon cells that will link muscles to the axial skeleton¹⁵. Here we have also addressed the relationship of the sclerotome with the ventral cell clusters of the caudal somites that give rise to the SCPs.

Activated leukocyte cell adhesion molecule (Alcam or CD166) is a large cell surface glycoprotein of the immunoglobulin superfamily that mediates adhesion through homophilic interactions in various tissues¹⁶, and heterophilic interactions with CD6 at the interface of T cells and antigen-presenting cells¹⁷, and with galectin-8 in the extracellular matrix¹⁸. While expressed in a wide variety of tissues, Alcam is often found in cell subsets involved in dynamic growth and/or

¹Institut Pasteur, Department of Developmental & Stem Cell Biology, Paris 75015, France. ²INSERM, Paris 75013, France. ³CNRS, UMR3738, Paris 75015, France.

✉ e-mail: emur@pasteur.fr

migration processes including neural development¹⁹, pharyngeal pouch formation²⁰, angiogenesis¹⁸, kidney development²¹, and tumor progression²²; it is also found in mesenchymal stromal cells of bone marrow and fetal liver^{23–25}. The short cytoplasmic tail of Alcam was shown to interact indirectly with the actin cytoskeleton via actin-binding proteins such as ezrin and syntenin-1²⁶. These interactions of the cytoplasmic domain dynamically regulate the clustering of Alcam molecules at the cell surface and the strength of the homophilic and heterophilic interactions^{27,28}.

Platelet-derived growth factor receptor α (PDGFR- α) is a highly conserved receptor tyrosine kinase. The binding of PDGFs to PDGF receptors induces their dimerization, which unlocks their tyrosine kinase activity and results in the autophosphorylation of specific tyrosine residues, which then act as binding sites for intracellular Src homology 2 (SH2) domain-containing signaling molecules^{29,30}. PDGFR- α mediated signaling regulates various processes of embryonic development and organogenesis, notably the proliferation then migration, and differentiation of specialized mesenchymal cells in various organ anlagen³¹. PDGFR- α is also a marker of bone marrow stromal cells, that has been widely used to purify them^{32,33}.

Here we identify Alcam and Pdgfr- α as two essential transmembrane proteins in the process of SCP emergence from somite epithelial cells, their subsequent migration to become stromal cells, and the resulting structure and functionality of the CHT niche. We further show that the somite ventral clusters giving rise to them coincide with the caudal sclerotome and that Alcam and Pdgfr- α are similarly important for the emergence from the trunk somites of sub-aortic mesenchymal cells that foster the emergence of HSPCs from the aorta floor.

Results

Alcam is required for stromal cell development from somites

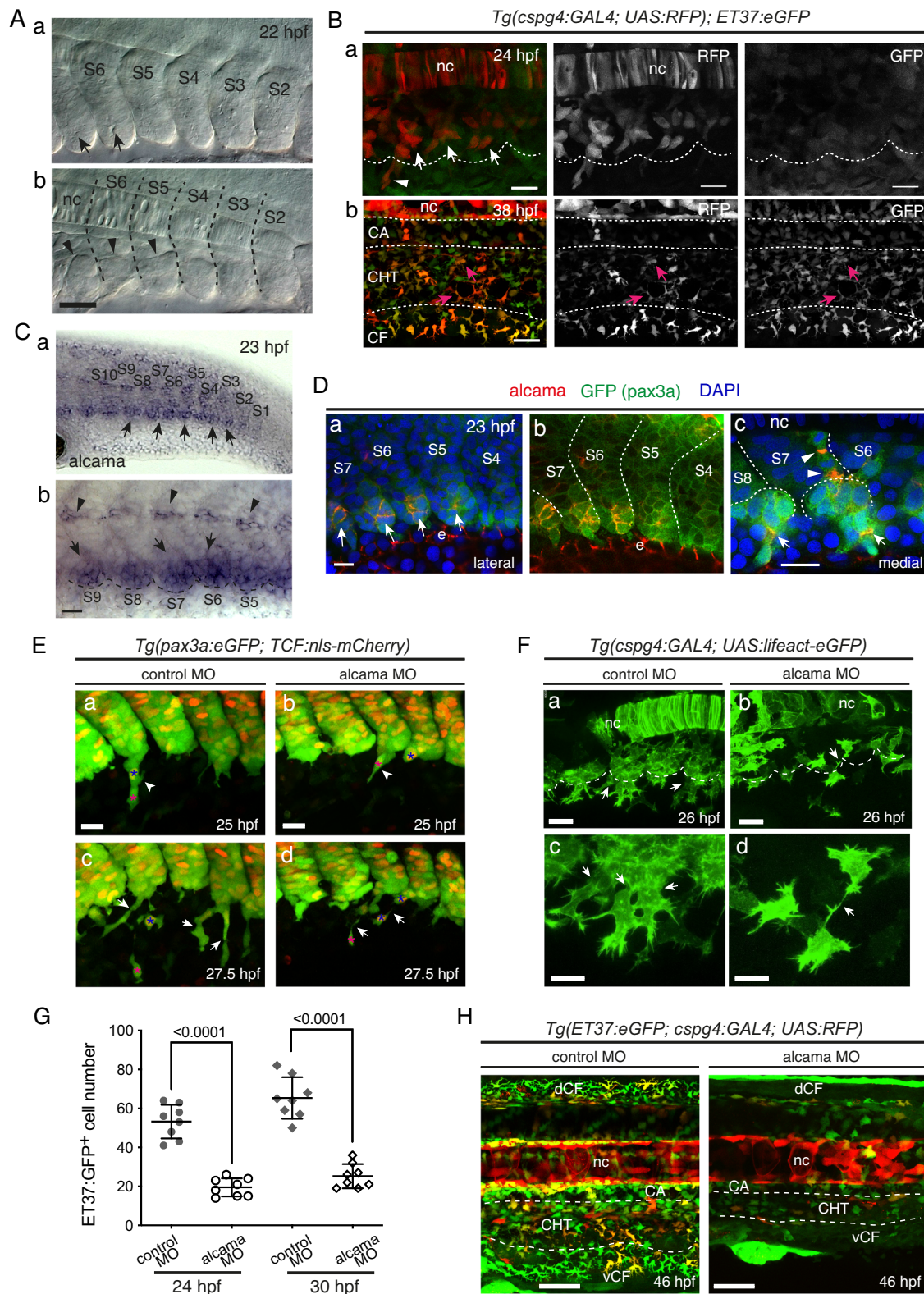
We previously described that cell clusters containing SCPs appeared at the ventral side of caudal somites by 21–22 hpf⁷. More precisely, the relative timing of this process among caudal somites derives from the timing of somite formation, which occurs in the rostrocaudal direction, with one new somite forming every 30 min. To monitor their subsequent maturation, it is convenient to number somites dynamically, calling S1 the most recently formed somite, S2 its rostral neighbor formed 30 min earlier, and so on³⁴. Within this framework, we found that the ventral clusters (VC) first become apparent by live video-enhanced DIC/Nomarski (VE-DIC) microscopy in the transition from somite maturation stage S4–S5, hence 2.5 h after somite formation (Fig. 1A). During cluster formation, the cells located on the ventral side of the somites adopt a rosette-like structure with a small cavity in the center (Fig. 1A-a and Supplementary Movie 1). To visualize the subsequent emigration of SCPs from these VCs, we previously used TCF-driven fluorescent reporters expressed in all somite cells, which were merely inherited by the emigrating SCPs⁷. In the present study, to analyze the fate of these SCPs, we first used the *Tg(pax3a:eGFP)* and *Tg(ET37:eGFP)* lines³⁵. *Tg(pax3a:eGFP)* labeled somite cells weakly, then the VCs more strongly, as well as the migrating SCPs (Supplementary Movie 2) up to 2.5 dpf. The *Tg(ET37:eGFP)* line also highlights somite cells weakly³⁵, then starts to label SCPs more strongly as they start to emigrate from the somites (Supplementary Fig. 1A). We also aimed to create a new Tg line that would label SCPs more specifically and throughout their development. We first searched for genes that seemed specifically expressed in the VCs in the ZFIN whole-mount in situ hybridization (WISH) databank. Our subsequent study by WISH of candidate genes between 23 and 48 hpf led us to target the chondroitin sulfate proteoglycan 4 (*cspg4*) gene, which we found to be expressed in the VCs from somite maturation stage S6 onwards (Supplementary Fig. 1B). We thus generated a BAC-based Tg line expressing the GAL4 transcription factor (TF) from the *cspg4* regulatory regions. This *TgBAC(cspg4:Gal4)* line crossed with a

Tg(UAS:RFP) reporter line faithfully recapitulates the *cspg4* gene expression pattern spatiotemporally (Fig. 1B, Supplementary Fig. 1C–E), although expression is somewhat mosaic—a typical limitation of Gal4/UAS expression systems in zebrafish. With the exception of the notochord, in the caudal region RFP expression highlights the VCs and their derivatives. Upon live imaging of *Tg(cspg4:Gal4; UAS:RFP; ET37:eGFP)* embryos, we noticed that by 29 hpf, RFP⁺GFP⁺ cells were migrating towards not only the ventral but also the dorsal side (Supplementary Fig. 1C). The latter cell population migrated along the medial side of the somites towards the notochord, suggesting chondro-progenitor and/or tenocyte fates, hence sclerotomal nature^{9,10,15}. Ventral-wards migrating SCPs gave rise to stromal cells throughout the CHT by 38 hpf, and some migrated even further ventrally to become fin mesenchymal cells³⁵ (FMCs) in the caudal fin (Fig. 1B-b). These three fates of somite VC-derived cells are recapitulated in Supplementary Fig. 1F.

To understand how somite epithelial cells compartmentalize to give rise to the VCs and their derivatives, we also searched for cell adhesion molecules expressed specifically in the VCs. We found that the *alcam* gene (coding for activated leukocyte cell adhesion molecule a, aka CD166), was expressed in the VCs more strongly than in the bulk of the somites at 23 hpf, and its expression was already observed, albeit slightly, on the ventral side of somites from the S2/S3 stage, i.e. before cluster formation (Fig. 1C). Immunofluorescence allowed us to first detect the Alcam protein at the very core of the clusters as they first appeared morphologically, i.e. at somite stage S5 (Fig. 1D-a, b), suggesting post-transcriptional control of *alcam* expression at earlier somite maturation stages. Upon somite maturation to S6–S8, Alcam protein signals then gradually propagated to delineate cell boundaries within the clusters (Fig. 1D-a, b). We then detected the Alcam protein at joints between VC-derived cells migrating both ventral- and dorsal-wards (Fig. 1D-c). We examined the impact of *alcam* knock-down by using an antisense morpholino oligonucleotide (MO) that completely blocked translation of the *alcam* transcript in vivo (Supplementary Fig. 1G, H). The resulting morphant embryos had a globally normal development, somite VCs formed and cells began to emigrate from them. However, injection in *Tg(pax3a:eGFP; TCF:nls-mCherry)* embryos revealed that while in control embryos, SCPs initially migrated as strings of 2–3 cells interconnected by a rather large contact surface (Fig. 1E-a, c), which immunostaining showed to be enriched in Alcam protein (Fig. 1D-c), in *alcam* morphants, adhesion between migrating SCPs was reduced to a very small surface at the tip of an elongated cell protrusion (Fig. 1E-b, d). We next crossed our *TgBAC(cspg4:Gal4; UAS:RFP)* line with *Tg(UAS:Lifect-eGFP)*³⁶, in which Lifect-eGFP allows to highlight F-actin in vivo, so as to visualize actin dynamics and cellular projections during SCP emergence and migration. Lifect-eGFP⁺ VC-derived cells were clearly less numerous in *alcam* morphants by 26 hpf (Fig. 1F)—a finding confirmed in the *Tg(ET37:eGFP)* background (Fig. 1G). This reduced number was later mirrored by a similarly (2.7-fold) lower number of SCPs after migration into the CHT by 30 hpf (Fig. 1G), and a clearly lower number of both stromal cells in the CHT and FMCs by 46 hpf (Fig. 1H).

Alcam regulates the migration behavior of SCPs via F-actin

Time-lapse imaging of migrating Lifect-GFP⁺ SCPs in *alcam* morphants revealed a characteristic cell morphology compared to SCPs in control embryos (Fig. 2A). Filopodial projections in migrating leader SCPs usually occur mainly at the leading edge, whereas they were 50% more numerous (Supplementary Fig. 2A-a) and more randomly scattered around the migrating cell in *alcam* morphants (Fig. 2B). In addition, even though they were slightly longer on average in *alcam* morphants (Supplementary Fig. 2A-b), unlike in control embryos their length did not correlate with their position relative to the direction of migration (Fig. 2C). A further quantitative analysis of confocal live images showed that (i) a high Lifect-GFP (F-actin) signal was present



throughout migrating SCPs in *alcama* morphants whereas the F-actin signal was observed predominantly at the leading edge in controls (Supplementary Fig. 2B), and (ii) the surface area of migrating SCPs in *alcama* morphants was much larger than in controls (Supplementary Fig. 2C). These changes in morphology and F-actin distribution correlated with a strong defect in SCP migration, as their linear distance of migration in *alcama* morphants was less than half that in the control group (Fig. 2D). Later on, by 46 hpf, this migration defect had

translated in a much thinner distribution of ET37:eGFP⁺ stromal cells in the CHT (Fig. 1H).

To gain more insight into the implication of Alcama in SCP migration, we took advantage of the *Tg(cspg4:Gal4)* driver line to express specifically in these cells three different forms of Alcama fused to eGFP at its C-terminus—a WT full-length Alcama (Alcama-FL-eGFP), and two mutant forms: (i) Alcama-ΔN-eGFP, lacking both N-terminal Ig-like V-type domains that are known to mediate homophilic cell

Fig. 1 | SCP development and requirement for Alcama. **A** VE-DIC microscopy of developing caudal somites at 22 hpf, rostral to the left, dorsal to the top. Somites are numbered S2–S6 according to their maturation stage. Lateral (**a**) and more medial (**b**) focal planes show the central lumen (**a**, arrows) formed within the ventral somite clusters, and the dorsal border of the clusters (**b**, arrowheads). Dashed lines indicate intersomitic boundaries. Scale bar, 40 μ m. **B** Confocal projections of live *Tg(cspg4:Gal4; UAS:RFP; ET37:eGFP)* embryos at 24 (**a**) and 38 (**b**) hpf. **a** Arrows and arrowhead point at VC cells and an emerging SCP, respectively; the dotted line outlines the ventral border of caudal somites. Magenta arrows in **b** point at RFP/GFP double-positive cells in the CHT. Scale bars, 20 μ m. **C** WISH for alcama at 23 hpf. Wide-area image of the tail (**a**) and magnified view of the ventral part of somites S5–S9 (**b**). Arrows and arrowheads point at somite VCs and cells prefiguring the horizontal myoseptum, respectively; a dotted line outlines the somite ventral border; scale bar, 20 μ m. **D** Immunostaining for Alcama (red), pax3a:eGFP (green), together with DAPI (blue) at 23 hpf. **a** Overlay of red, blue and green signals; arrows point at Alcama labeling in the somite VCs. **b** Same image as **a** without DAPI staining; **c** epidermis. **c** At a deeper focal plane, strong Alcama signals were detected at contacts between cells migrating dorsal-wards (arrowheads) and ventral-wards (arrows); dashed lines delineate the VCs and somite borders. Scale

bars, 20 μ m. **E** Confocal maximum projections of control or alcama MO-injected *Tg(pax3a:eGFP; TCF:nls-mCherry)* embryos at 25 (**a**, **b**) and 27.5 (**c**, **d**) hpf. (**a**, **b**) Arrowheads show SCPs beginning to emigrate; magenta and blue asterisks point to the same cells as in (**c**) and (**d**), respectively. **c**, **d** Arrows point at intercellular junctions of migrating SCPs. $n = 12$ for each condition from four independent experiments. Scale bars, 25 μ m. **F** Confocal projections of control or alcama MO-injected *Tg(cspg4:Gal4; UAS:Lifeact-eGFP)* at 26 hpf. Dashed lines indicate the somite ventral borders. Arrows point at connections between migrating SCPs. Magnified images are shown in (**c**) and (**d**). $n = 9$ for each condition from three independent experiments. Scale bars, 20 μ m. **G** Quantification of ET37:eGFP⁺ cells in the ventral tail of live control and alcama MO-injected embryos, at 24 and 30 hpf over a 5-somites width ($n = 8$ embryos each; mean \pm SD; two-tailed Student's *t*-test, Source data are provided as a Source Data file). At 24 hpf, all GFP⁺ cells ventral to the notochord were counted; at 30 hpf, all GFP⁺ cells ventral to the somites were counted. **H** Confocal projections of control or alcama MO-injected *Tg(ET37:eGFP; cspg4:Gal4; UAS:RFP)* embryos at 46 hpf. Dashed lines delineate the CHT. $n = 10$ for each condition from a single experiment. Scale bars, 50 μ m. nc notochord, CA caudal artery, CHT caudal hematopoietic tissue, vCF and dCF ventral and dorsal caudal fin.

adhesion³⁷ and (ii) Alcama- Δ PDZ-eGFP, in which we introduced in the short cytoplasmic domain of Alcama three amino acid changes predicted to suppress the binding of PDZ domain-containing proteins (Supplementary Fig. 2D), such as syntenin²⁶. These different forms were inserted downstream of a UAS promoter, and the constructs were injected in *Tg(cspg4:Gal4; UAS:RFP)* embryos, leading to specific but mosaic expression of the GFP-linked mutant forms of Alcama among VC-derived cells. Expression of Alcama-FL-eGFP in the VCs did not perturb SCP emergence and migration (Supplementary Fig. 2E, Supplementary Movie 3). In contrast, SCPs expressing Alcama- Δ N-eGFP appeared disconnected from their neighbors within the VCs, and soon developed intense filopodial dynamics while still within the somite (Fig. 2Ea–c, Supplementary Movie 4), but most often with no resulting ventral-wards migration towards the CHT, whereas internal control neighboring RFP⁺GFP⁺ cells migrated normally (Fig. 2E–d). Alcama- Δ PDZ-eGFP⁺ VC cells and their SCP derivatives displayed much fewer filopodia compared to WT or Alcama- Δ N-eGFP expressing cells; they still showed some GFP enrichment at cell-cell contacts, but no clear polarity (Fig. 2Fa–c, Supplementary Movie 5). Like Alcama- Δ N-eGFP expressing cells, Alcama- Δ PDZ-eGFP⁺ SCPs barely migrated to the ventral side, compared with (RFP⁺GFP⁺) SCPs in the same embryo (Fig. 2F–d). In contrast, the dorsal-wards migration of VC-derived GFP⁺ cells was rather retained in both cases, as well as for Alcama-FL-eGFP expressing cells (Fig. 2G and Supplementary Fig. 2F, G). In vivo tracking of GFP⁺ cells in both Alcama- Δ N-eGFP and - Δ PDZ-eGFP expressing embryos confirmed that the cells that egressed ventrally from the VCs then wandered around and migrated only shortly toward the ventral side, whereas the dorsal-wards migration was similar to that of control or Alcama-FL-eGFP expressing cells (Fig. 2H, I). Statistical analysis of their fates confirmed that the phenotype of GFP⁺ mutant cells was predominantly ‘immobile’ or ‘dorsal migration’, with occasional ‘ventral migration’ limited to a short distance (Fig. 2J). Altogether, these data show that Alcama is cell-autonomously involved in SCP emergence and migration.

Alcama and PDGFR- α deficiency similarly affect SCP development

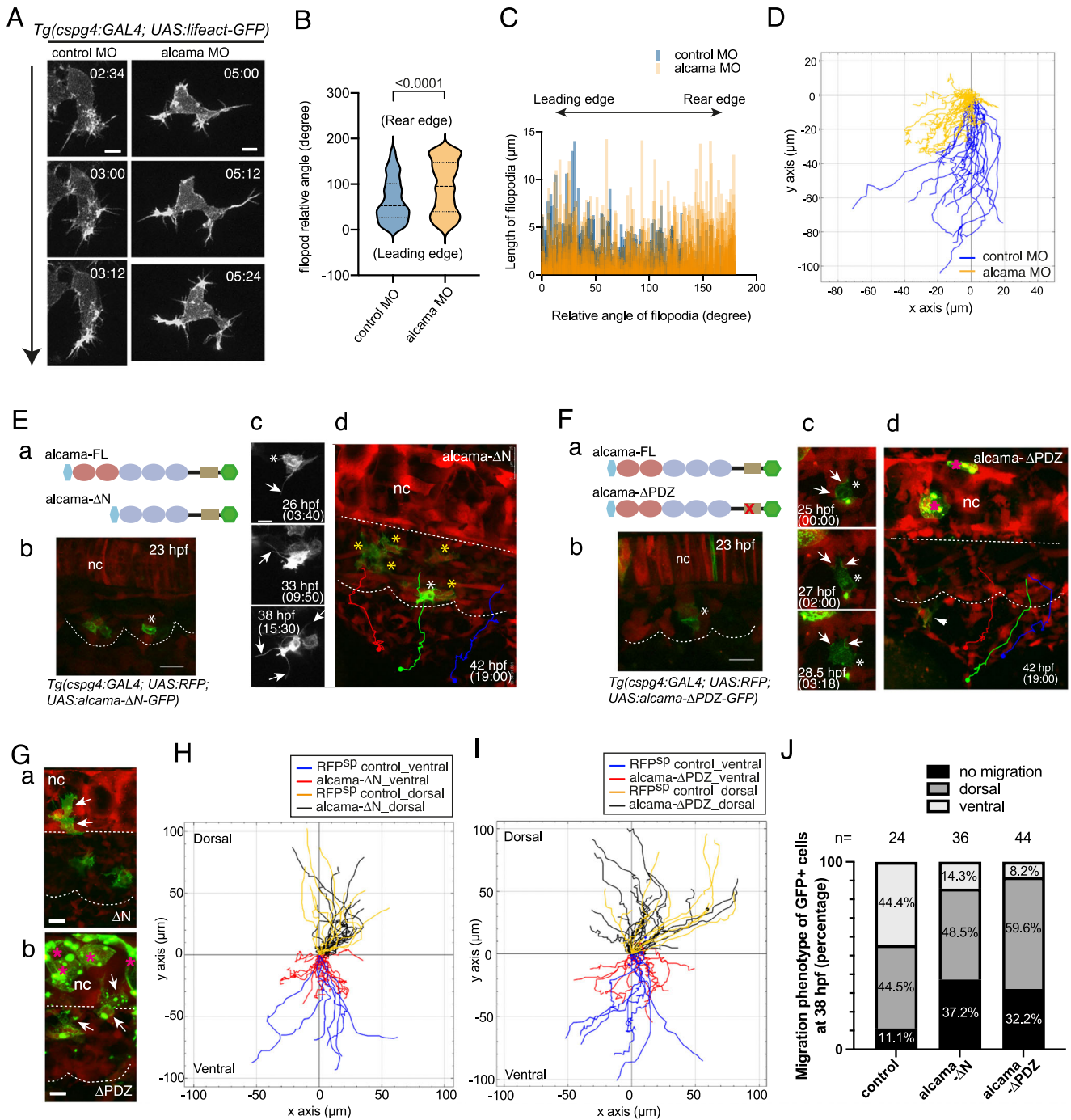
A prominent feature of alcama morphant and dominant-negative mutant phenotypes was the inhibition of SCP ventral migration. Therefore, we investigated the gene expression of receptors for cytokines and growth factors that might be involved in SCP migration. We found that *pdgfr- α* was specifically expressed in the somite VCs, starting by somite maturation stage S6, and then in the migrating cells derived from them (Fig. 3F–a, b). Therefore we hypothesized a possible cross-talk between Alcama and Pdgfr- α . It is known that PDGF signaling

leads to an increase in AKT and ERK phosphorylation^{38,39}. We first investigated the impact of *alcama* knockdown on pERK signaling in the caudal region at 26 hpf. The number of pERK⁺ cells was reduced to 36% of control level in the CHT of alcama morphants, while it recovered to almost the control level in the rescued group (Fig. 3A). Then, we investigated the impact of Pdgfr- α deficiency, using a previously validated MO against *pdgfra*⁴⁰. First, we analyzed the colocalization of pERK-positive cells with SCPs marked by pax3a-GFP in alcama and *pdgfra* morphants. While in control embryos we could observe pERK⁺GFP⁺ migrating SCPs, in alcama and *pdgfra* morphants the overall number of pERK⁺ cells was reduced, and no pERK signal was observed among migrating SCPs (Supplementary Fig. 3A). Time-lapse imaging of SCP emergence in *pdgfra* morphants by 23–24 hpf revealed that the cohesion of the VCs was compromised, with groups of cells often delaminating together from the somite (Supplementary Fig. 3B), and then several SCPs per somite cluster or cell group starting to emigrate simultaneously (Fig. 3B), yet with a clearly reduced migration efficiency relative to WT embryos. Quantification showed that the numbers of CHT stromal cells and FMCs originating from SCPs were reduced 2.4-fold and 2.0-fold, respectively, in *pdgfra* morphants by 40 hpf (Fig. 3C), similar to what we previously found for alcama morphants (Fig. 1G, H). Live imaging also showed that like in alcama morphants, the extent of ventral-wards migration of SCPs by that time was much reduced in the *pdgfra* morphants (Supplementary Movie 6). This impacted the co-migration of endothelial cells that made the caudal venous (CV) plexus, resulting in a much thinner plexus, often reduced to a single convoluted tube, in apposition to the overlying caudal artery, which could locally show a reduced diameter (Fig. 3D).

We then attempted to identify PDGF ligands that would activate Pdgfr- α signaling in the VCs and migrating SCPs. We performed pERK immunostaining on embryos overexpressing either of three different PDGFs which we had found by WISH to be more specifically expressed in the ventro-caudal area (Supplementary Fig. 3C). All three ligands activated pERK signaling, hence likely Pdgfr- α signaling, but the effect of Pdgfaa and Pdgfab was statistically more significant than Pdgfbb (Supplementary Fig. 3D).

PDGFR- α drives SCP migration through PI3K signaling

PI3K signaling is known to be activated downstream of various growth factor receptors including PDGF receptors⁴¹ following their activation. Pharmacological inhibition of PI3K isoforms using AS605240 (inhibiting PI3K isoforms γ , α), LY294002 (inhibiting isoforms α , β , δ), or CALI01 (inhibiting isoform δ) revealed that the migration of SCPs was compromised in embryos treated with LY294002, and more so with AS605240, resulting in a 3.5-fold reduction in stromal cell numbers by



40 hpf (Fig. 3E), whereas *pax3a*-GFP^{high} neural crest cells migrated with only a slight delay (Supplementary Fig. 3E, blue arrows). To monitor the migration of SCPs and other VC-derived cells over longer intervals, AS-treated embryos were fixed and labeled with a *pdgfra* in situ probe at stages encompassing the entire migration process. In the control group, dorsal-wards migration of VC-derived cells had already started by 23 hpf, whereas no migration was observed in the AS-treated embryos (Fig. 3F-a, c). By 36 hpf, SCP migration had not started yet in the AS-treated group, in which SCPs accumulated at the zone of their emergence, while it was already complete in the control group (Fig. 3F-b, d).

Since the involvement of PI3K in SCP migration was revealed, we then mutated two tyrosine residues in the intracellular domain of *Pdgfr- α* that are responsible for the binding of class IA ($\alpha/\beta/\delta$) PI3K to *Pdgfr- α* following its activation and autophosphorylation³⁸ (Fig. 4A),

and we cloned the mutated or WT *pdgfra* ORF followed by a tandem HA-tag downstream of a *hsp70* promoter⁴² (*hsp70:pdgfra- Δ PI3K-HA* or *hsp70:pdgfra^{WT}-HA*, respectively). Transient transgenics resulting from injection of the *hsp70:pdgfra- Δ PI3K-HA* or *hsp70:pdgfra^{WT}-HA* construct in *Tg(pax3a:eGFP)* embryos were heat-shocked at 19–20 hpf, then imaged in vivo from 23 hpf, or fixed for immunofluorescence at the same time point. The anti-HA antibody signals sometimes showed a mosaic distribution, but were sufficiently present in the targeted tissue of *hsp70:pdgfra- Δ PI3K-HA* and *hsp70:pdgfra^{WT}-HA* embryos at 24 hpf (Supplementary Fig. 4A). Heat-shocked *hsp70:pdgfra- Δ PI3K-HA* embryos typically showed a less clear outline of the somite VCs than controls. In addition, 38% of them showed multiple SCPs simultaneously initiating migration from one somite, reflecting the lack of leader cell, and 20.5% had at least one somite showing an ‘overflow’ phenotype in which the VC collectively delaminated into the ventro-

Fig. 2 | Alcama regulates SCP migration. **A** Time-lapse confocal images of a migrating SCP leader cell from control or *alcama* MO-injected *Tg(cspg4:Gal4; UAS:Lifeact-GFP)* embryos around 28 hpf. The time after initiation of SCP migration is shown in the upper right corner of each panel. The time lag between control and *alcama* morphant SCP is because the latter tend to take more time to fully egress from the somite. Arrow indicates the direction of migration. Scale bars, 10 μ m. **B** Violin plot of filopodia angles relative to the direction of migration for leader SCPs in control and *alcama* morphant embryos ($n = 7$ SCPs for each group, from 3 independent experiments; median \pm SD; two-tailed Mann–Whitney test). **C** Filopodia length as a function of their relative angles for leader SCPs in control and *alcama* morphants. **D** Overlay of individual tracks of control and *alcama*-deficient SCPs during their migration toward the CHT. (x,y) coordinates of the SCPs' starting points at somite borders are set to (0,0) and negative or positive values on the y-axis indicate ventral-wards or dorsal-wards migration, respectively. $n_{Exp} = 4$, $n_{embryos} = 6$, $n_{tracked\ cells} = 19$ and 17 for control or *alcama* morphants, respectively. **E, F** **a** Schematic representation of Alcama-FL-eGFP, Alcama- Δ N-eGFP (**E-a**) and Alcama- Δ PDZ-eGFP (**F-a**) mutant constructs. Pink and blue ovals indicate the V-type and C2-type Ig-like domains, respectively; the beige rectangle represents the short cytoplasmic domain. In (**F-a**), the red x indicates the mutated PDZ binding motif. Light blue and green hexagons represent the signal peptide and GFP, respectively. **E-b** Appearance of Alcama- Δ N-eGFP⁺ SCPs at 23 hpf. White asterisk indicates the same cell as shown in (**E-c**, **d**). Dotted lines delineate somite and notochord borders. Scale bar, 20 μ m. **c** Morphological evolution over 15.5 h of the Alcama- Δ N-eGFP⁺ SCP shown in (**E-b**) (see also Supplementary Movie 4). Scale bar, 10 μ m. **E-d** End point of the time-lapse imaging shown in (**E-b**, **c**) and Supplementary

Movie 4. GFP⁺ SCPs marked by yellow asterisks did not migrate out of the somites, whereas RFP⁺/GFP⁺ WT SCPs showed a normal emigration pattern exemplified by the three colored trajectories. A straight dotted line indicates the notochord lower border. **F** (**b**) Appearance of Alcama- Δ PDZ-eGFP expressing VC cell (asterisk) at 23 hpf, followed over time in (**c**) (see also Supplementary Movie 5). Scale bar, 20 μ m. **c** Arrows point at large contact areas between the GFP⁺ cell and RFP⁺ cells. **d** End point of the time-lapse imaging of the same embryo; the GFP⁺ SCP followed up in (**b**, **c**) had disappeared by 42 hpf, while another such cell displayed short-distance migration (arrowhead). RFP⁺/GFP⁺ (WT) SCPs showed a normal emigration pattern indicated by three colored trajectories. Straight and curvy dashed lines delineate the ventral border of notochord and somites. **G** Dorsal-wards migration of Alcama- Δ N-eGFP and - Δ PDZ-eGFP expressing cells (arrows) by 27 hpf. Scale bars, 10 μ m. Magenta asterisks in (**F-d**) and (**G-b**) label GFP⁺ notochord cells. **H** Overlay of individual tracks of control (RFP⁺/GFP⁺ SCPs; orange and blue lines) and Alcama- Δ N-eGFP expressing SCPs (black and red lines). $n_{Exp} = 5$, $n_{embryos} = 7$, $n_{tracked\ cells} = 29$ and 17 for Alcama- Δ N-eGFP⁺ and control RFP⁺/GFP⁺ SCPs, respectively. **I** Overlay of individual tracks of control (RFP⁺/GFP⁺ SCPs; orange and blue lines) and Alcama- Δ PDZ-eGFP⁺ SCPs (black and red lines). $n_{Exp} = 4$, $n_{embryos} = 5$, $n_{tracked\ cells} = 32$ and 17 for Alcama- Δ PDZ-eGFP⁺ and control SCPs, respectively. **J** Frequency histogram of D/V migration patterns of Alcama- Δ N-eGFP⁺ and - Δ PDZ-eGFP⁺ cells compared with GFP⁺ cells of *Tg(cspg4:Gal4;UAS:GFP)* embryos at 38 hpf. The number of embryos analyzed was 24 (WT), 36 (Alcama- Δ N), and 44 (Alcama- Δ PDZ) from three independent experiments. nc notochord. Source data for **B**, **C**, **D**, **H**, **I**, and **J** are provided as a Source Data file.

caudal cavity, reminiscent of the phenotype observed above in *pdgfra* morphants (Supplementary Fig. 4B); these cell populations tended to disperse over time but did not go through the normal migration process (Fig. 4B-b, c). In embryos overexpressing the *pdgfra*^{WT}-HA construct, more apoptotic bodies were detected than in WT embryos, but no abnormalities were observed in the VCs and emigration of SCPs (Fig. 4B-a). Interestingly, the morphology of migrating SCPs in *pdgfra*- Δ PI3K expressing embryos was quite similar to that observed in *alcama* morphants, with long and numerous filopodia and the cell's main axis often orthogonal to the ventral-wards direction of migration (Fig. 4C, Supplementary Movie 7), and with increased 3D cell surface area and volume (Supplementary Fig. 4C, D). Importantly, the number of VC-derived GFP⁺ cells was clearly more decreased for those migrating ventral-wards (SCPs) than for those migrating dorsal-wards (DMCs) (Fig. 4D), again as previously observed upon Alcama deficiency. The total number of SCPs at 36 hpf in the CHT of *pdgfra*- Δ PI3K expressing embryos was also strongly reduced (Fig. 4E), as in Alcama- or *Pdgfra*-deficient embryos.

We then checked whether the application of CRISPR/Cas9 technology to the *alcama* and *pdgfra* genes would confirm our findings. To mimic the genetic modification introduced by *alcama* and *pdgfra* MOs, gRNAs were designed to delete the promoter of the *alcama* gene (Supplementary Fig. 5A-a) and the intron2–exon3 splice junction of the *pdgfra* gene (Supplementary Fig. 5B-a). Genomic PCR and subsequent sequencing on individual *alcama* gRNA injected embryos indicated *alcama* promoter deletion in 8/12 embryos (Supplementary Fig. 5A-b). A similar analysis on *pdgfra*-gRNA injected embryos indicated *pdgfra* intron2–exon3 splice junction deletion in 10/16 embryos (Supplementary Fig. 5B-b left panel), and cDNA analysis on pooled *pdgfra*-gRNA injected embryos confirmed exon3 deletion in the resulting mRNA (Supplementary Fig. 5B-b right panel). The phenotypic consequences were analyzed in the *Tg(pax3a:eGFP; kdr1:ras-mCherry)* background. Relative to control embryos, *alcama* and *pdgfra* crispants both showed a greatly reduced number of *pax3*:GFP⁺ stromal cells in the CHT at 48 hpf (Supplementary Fig. 5C), and a malformed CV plexus often reduced to a single large convoluted tube (Supplementary Figs. 5D, E), similar to what we previously described for the morphants. Thus *alcama* and *pdgfra* crispants confirmed our previous findings using *alcama* and *pdgfra* morphants.

Caudal somite ventral clusters coincide with the sclerotome

Since our live imaging revealed that the somite VCs from which SCPs originate also gave rise to cells migrating dorsal-wards towards the notochord, it suggested an overlap or identity of somite VCs with the sclerotome. We examined this point through a double WISH for the sclerotome marker *nkx3.1*¹⁵ and RFP expressed in *Tg(cspg4:Gal4; UAS:RFP)* embryos. This revealed a complete coincidence of both stainings in the tail, hence the identity of the somite VCs with the sclerotome (Fig. 5A). We further examined the *Tg(ola-twist:Gal4; UAS:Kaede)* line, which has been used to trace sclerotome-derived cells in zebrafish. We found that Kaede expression in the tail at 24 hpf indeed covered a large subset of the *nkx3.1/cspg4:Gal4* expression domain, starting only a bit later in somite maturation, by stage S8 (Fig. 5B). We then photoconverted Kaede in single expressing cells at the ventral border of the four anterior-most caudal somites at 23 hpf (which at that time represent somite maturation stages S8–S11), and tracked their fate up to 48 hpf (Fig. 5C, D). Three main fates were equally represented—stromal cells of the CHT (33%), DMCs (31%), and muscle fibers (31%), while the FMC fate was more marginal (5%) (Fig. 5E). This cell fate analysis thus confirmed our previous findings, but added the muscle fiber category, reminiscent of the pioneer study by Morin-Kensicki et al.⁹ who found that the posterior part of each ventro-medial cell cluster gave rise to some muscle cells in addition to the typical sclerotome fates (Fig. 5F). Only SCP fated cells underwent mitosis during the observed period (4/14), and they did so on their way to or within the CHT; therefore all photoconverted cells showed only one fate during the tracked period, suggesting that cell fate within the VCs may already be restricted by somite stage S8 (the earliest stage at which Kaede was sufficiently expressed for photoconversion-based cell tracking).

Alcama and Pdgfr- α expression are regulated by sclerotomal transcription factors

Our WISH analysis revealed that other TFs considered as sclerotome markers within the somites, such as *Pax9*, *Snai2*, *Twist1a*, and *Twist1b* were expressed in the VCs of caudal somites from somite stage S5/S6, and also quite earlier—from S1—for *Snai2* (Fig. 6A). Therefore, we investigated if these TFs regulate the expression of *alcama* and *pdgfra* during SCP development. To this end, we first isolated promoter regions of the *alcama* (3.3 kb) and *pdgfra* (3.2 kb) genes from BACs and

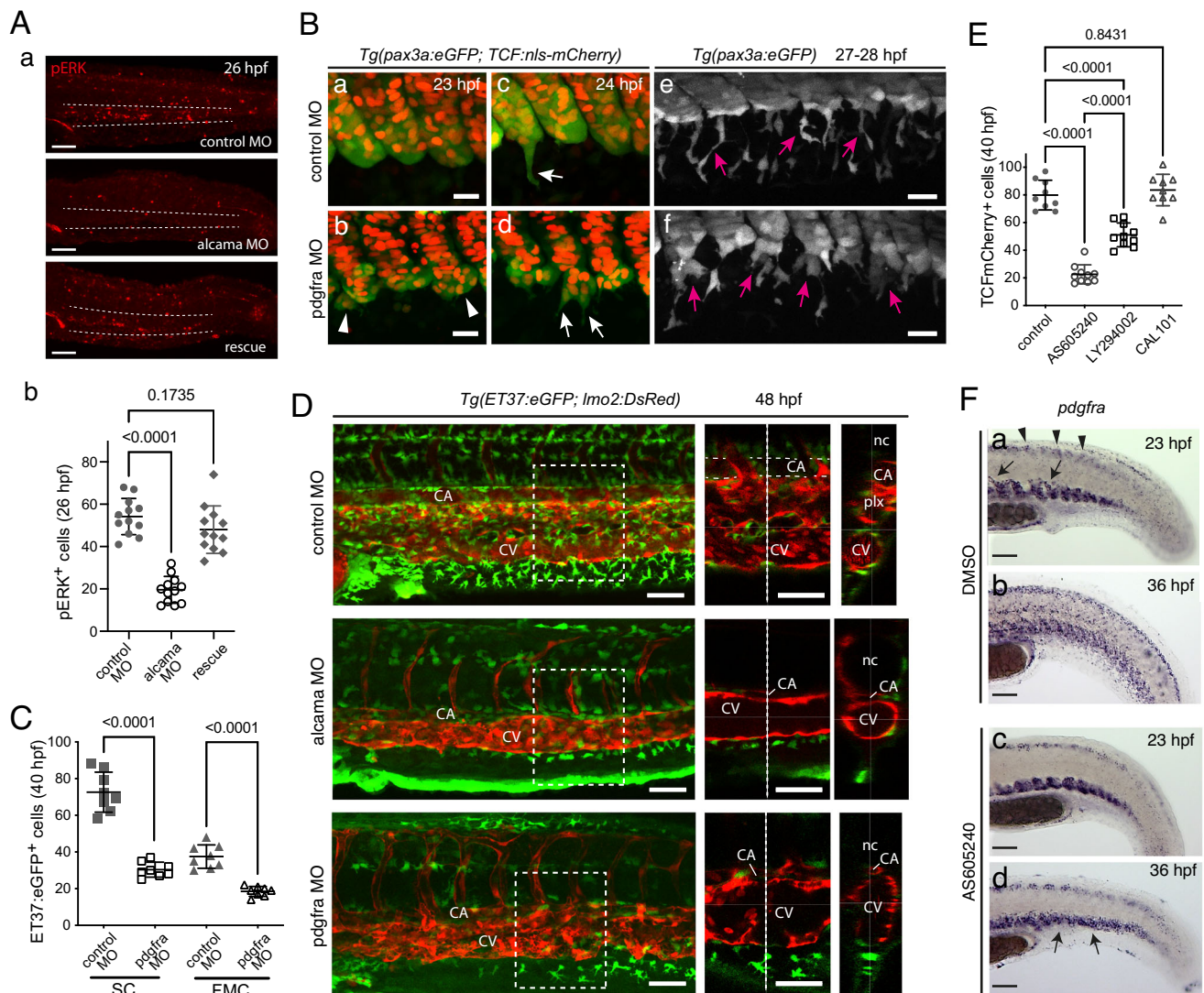


Fig. 3 | Pdgfr- α /PI3K signaling regulates SCP migration. **A** (a) Immunofluorescence for pERK at 26 hpf in the tail region of embryos injected with control MO, alcama MO, or alcama MO + alcama mRNA (“rescue”); $n = 12$ embryos from two independent experiments. Dashed lines indicate the CHT border. **b** Quantification of **a** ($n = 12$ embryos for each group; mean \pm SD; one-way ANOVA followed by Dunnett’s multiple comparison test). **B** Confocal projections of live control (**a, c, e**) or *pdgfra* (**b, d, f**) MO-injected *Tg(ET37:eGFP; TCF:nls-mCherry)* embryos from 23 to 28 hpf. Arrowheads point at cohesion defects observed in the VCs of *pdgfra* MO-injected embryos. White and magenta arrows indicate emerging (**c, d**) and migrating (**e, f**) SCPs, respectively; $n = 9$ for each condition from three independent experiments. Scale bars, 25 μ m. **C** Quantification of ET37:eGFP⁺ stromal cells and FMCs in control and *pdgfra* MO-injected embryos at 40 hpf ($n = 8$ for each group, from the same experiment; mean \pm SD; two-tailed Student’s *t*-test). **D** Confocal maximum projections of control, alcama, and *pdgfra* MO-injected *Tg(ET37:eGFP;*

lmo2:DsRed) embryos at 48 hpf. An enlarged view of the area enclosed by the dashed square is shown in the middle panel (single slice image), where a dotted vertical line shows the position of the orthogonal projection (transverse section) shown in the right panel; $n = 6$ for each condition from three independent experiments. Scale bars, 50 μ m. **E** Quantification of TCF:nls-mCherry⁺ stromal cells in the CHT of control embryos ($n = 9$), or embryos treated from 20 hpf with AS605240 ($n = 10$), LY294002 ($n = 10$), or CAL101 ($n = 9$) at 40 hpf (mean \pm SD; one-way ANOVA followed by Tukey’s multiple comparison test). **F** WISH for *pdgfra* at 23 and 36 hpf in 0.2% DMSO (control) and AS605240-treated embryos. Arrows and arrowheads in **(a)** indicate VC cells migrating toward the notochord and dorsal mesenchymal cells at 23 hpf, respectively. Arrows in **(d)** show SCPs slightly dispersed around the VCs at 36 hpf. $n = 12$ for each condition from two independent experiments. CA caudal artery, CV definitive caudal vein, Plx venous plexus, nc notochord. Source data for **A-b, C,** and **E** are provided as a Source Data file.

cloned them into the pGL3 Basic vector to monitor their promoter activity in vivo in various conditions through a Dual luciferase assay performed on tail lysates at 23 hpf (Fig. 6B-a, E-a). Co-injection of the pGL3-alcama-luc construct with either *snai2* MO or *pax9* mRNA attenuated the alcama promoter activity, while co-injection with *snai2* mRNA or *pax9* MO had no significant effect (Fig. 6B-b). Consistent with this, alcama mRNA expression in the tail of *pax9* morphants was upregulated at 24 hpf (Fig. 6C), while it was down-regulated in the tail of *snai2* morphants (Fig. 6G). We similarly analyzed the effects of *twist1a/twist1b* and *snai2* on the *pdgfra* promoter by co-injection with pGL3-*pdgfra*-luc. Double knockdown of *twist1a* and *1b* led to a drastic

decrease in *pdgfra* promoter activity in the tail samples, whereas co-injection of *twist1b* mRNA stimulated it (Fig. 6E-b). In line with this, *pdgfra* mRNA expression in the tail was downregulated in *twist1a/1b* morphants (Fig. 6F). *Snai2* MO also reduced *pdgfra* promoter activity (Fig. 6E-b), and consistently, *pdgfra* expression in the tail of *snai2* morphants was significantly reduced (Fig. 6G). Finally, we found that these sclerotomal TFs regulated each other in the tail, as *pax9* knockdown upregulated *snai2* expression but downregulated *twist1b*, while *snai2* knockdown down-regulated *pax9* (Fig. 6D, G). The network of genetic interactions deduced from all these data is depicted in Fig. 6H.

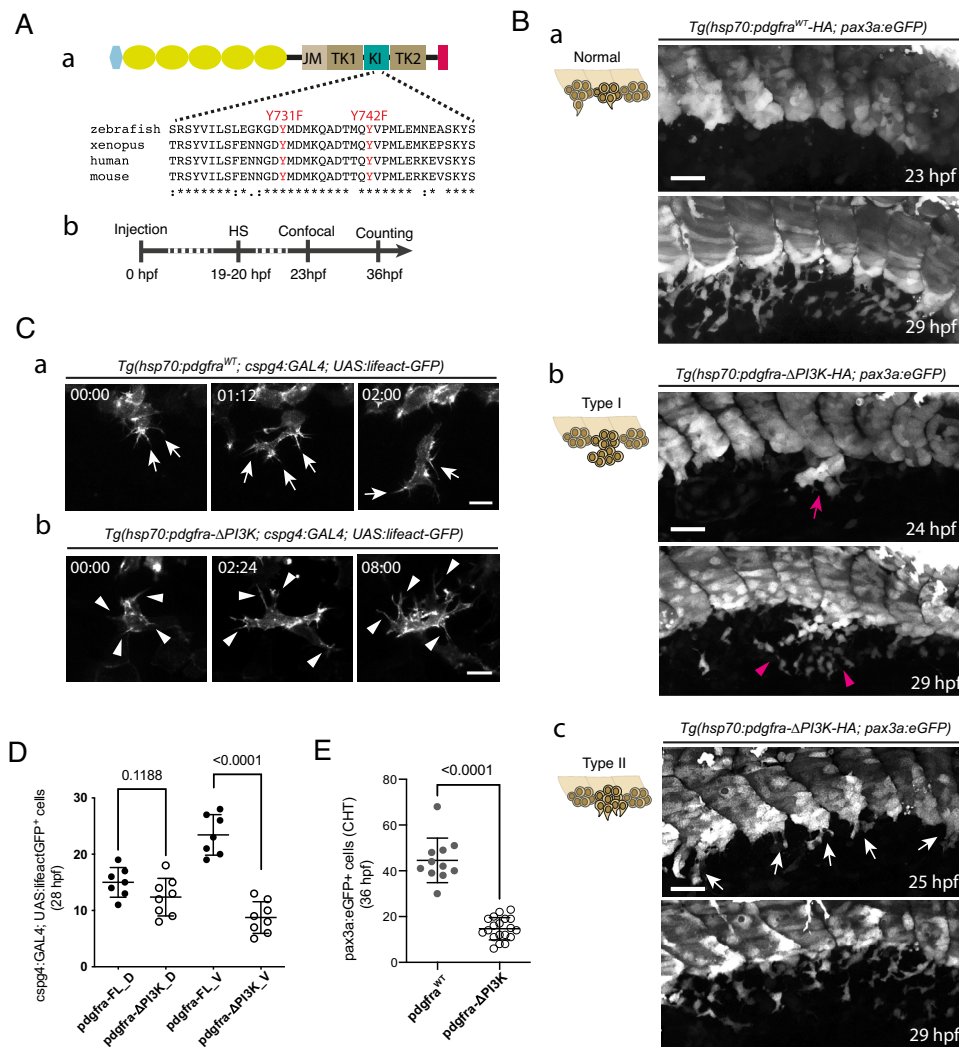


Fig. 4 | Pdgfr- α influences cluster cohesion and SCP migration behavior through PI3K binding. **A** (a) Schematic representation of Pdgfra fused to tandem HA-tag (red) at its C-terminus, and amino acid alignment around the site of mutations in the KI (kinase insert) domain. The light blue hexagon and yellow ovals indicate the signal peptide and Ig-like extracellular domains, respectively; JM juxtamembrane, TK1 tyrosine kinase domain 1, TK2 tyrosine kinase domain 2, tyrosine residues involved in PI3K binding when phosphorylated that we mutated into phenylalanines are shown in red. **b** Time course of the experiment; HS, heat-shock. **B** Confocal projections at 23 and 29 hpf of live *Tg(pax3a:eGFP)* embryos injected with *hsp70:pdgfra^{WT}-HA* (a) or *hsp70:pdgfra- Δ PI3K* construct (b, c) and heat-shocked at 19–20 hpf; *Tg(hsp70:pdgfra- Δ PI3K; pax3a:eGFP)* embryos show defects in VC cohesion (type I, b) or SCP emergence and migration (type II, c) (see also Supplementary Fig. 4B). Arrow in b indicates SCPs overflow out of the cluster before migration initiation. This cell population was dispersed locally after 5 hrs (arrowheads). c, Arrows indicate multiple SCPs emerging simultaneously from the

cluster; $n = 29$ (a), 7 (b), and 13 (c) for each condition from 9 independent experiments. Scale bars, 40 μ m. **C** Representative frames of a confocal time-lapse sequence starting at 23 hpf of a migrating SCP leader cell in *Tg(cspg4:GAL4; UAS:lifect-eGFP)* embryo injected with the *hsp70:pdgfra-FL* (a) or *hsp70:pdgfra- Δ PI3K* (b) construct. Time is indicated in hrs and min. Arrows in a indicate filopodia projected in the direction of migration; arrowheads in b indicate filopodia in all directions. Scale bars, 25 μ m. **D** Quantification of *Tg(cspg4:Gal4; UAS:lifect-eGFP)*⁺ SCPs migrating dorsal-wards (D) or ventral-wards (V) in *Pdgfra-FL* (control) and *Pdgfra- Δ PI3K* expressing embryos at 28 hpf ($n = 7$ and 8 embryos for control and *hsp70:pdgfra- Δ PI3K*, respectively, from 3 independent experiments. mean \pm SD; two-tailed Student's *t*-test. **E** Counting of *pax3a:eGFP*⁺ SCPs in control and *hsp70:pdgfra- Δ PI3K* embryos in the CHT at 36 hpf over a 5-somite width ($n = 11$ and 19 embryos for control and *hsp70:pdgfra- Δ PI3K*, respectively, from 3 independent experiments). mean \pm SD; two-tailed Student's *t*-test. Source data for **D** and **E** are provided as a Source Data file.

Recently Huang and coworkers found that in addition to the ventral sclerotome found in all vertebrates, zebrafish (and likely other finned vertebrates) possesses a smaller, dorsal sclerotome domain, mirroring the position of the ventral one, i.e. positioned at the dorsal-most border of the somites¹⁵. This domain is also marked by the classical sclerotome transcription factors, and notably gives rise to the FMCs of the dorsal side of the caudal fin, as well as tenocytes¹⁵ and ISV-associated pericytes and fibroblasts¹², as the ventral sclerotome does. We noted that *alcama* and *pdgfra* are both expressed in this dorsal sclerotome compartment as well as in the ventral one (Figs. 1C, 3F, and 7A, arrowheads) and that *Alcama* or *Pdgfra* or PI3K signaling deficiency all caused a strong reduction of FMCs in the dorsal side of the caudal

fin (Figs. 1H, 3F, Supplementary Figs. 3E and 5D, arrowheads), mirroring what we described above for the ventral sclerotome and ventral side of the caudal fin.

Trunk somites produce *alcama* and Pdgfr- α dependent stromal cells that foster HSPC emergence

Like the sclerotomal TFs mentioned above, *alcama* and *pdgfra* expression is not restricted to the tail, but also extends to the somites of the trunk (Fig. 7A). Moreover, as in the tail, *pax3a:eGFP*⁺ or *ET37:eGFP*⁺ mesenchymal cells are present in the trunk by 26 and 36 hpf, notably just lateral or ventral to the dorsal aorta (DA), and in close contact with it or with the dorsal wall of the underlying axial vein (PCV)

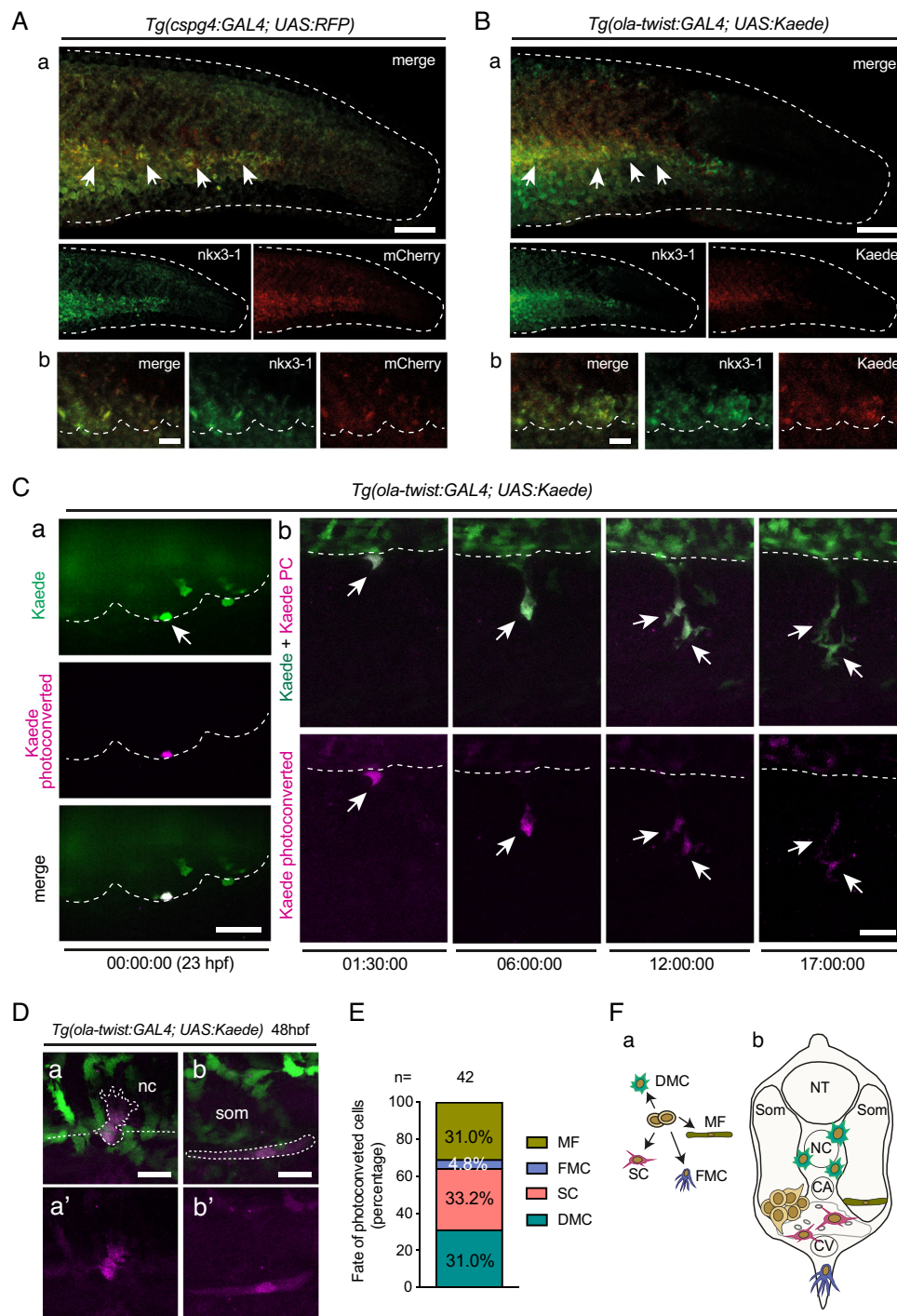


Fig. 5 | Somite VCs coincide with the sclerotome. **A, B** *Tg(cspg4:Gal4; UAS:RFP)* embryos (**A**) and *Tg(ola-twist:Gal4; UAS:Kaede)* embryos (**B**) were fixed at 24 hpf and subjected to double fluorescence WISH using probes for *nkx3.1* and *mCherry* or *Kaede* mRNA, respectively. The entire tail area (**a**) and magnified images of the VCs (**b**) are shown; dashed line and arrows in **a** indicate the border of the caudal region and VC cells showing double staining. Dashed lines in **b** delineate the VC ventral borders. Scale bars, 100 μ m in (**a**) and 20 μ m in (**b**). **C** Confocal images of a live *Tg(ola-twist:Gal4; UAS:Kaede)* embryo. **a** a single *Kaede*(green)⁺ cell at the ventral border of an anterior caudal somite was photoconverted (magenta) at 23 hpf. **b** Representative frames from a time-lapse follow-up of the *Kaede*⁺ cell photoconverted in (**a**), which underwent mitosis at 10h15 (~33 hpf). Dashed line

delineates the somite ventral border. Scale bars, 20 μ m. **D** examples of photoconverted cells that migrated dorsalwards to the notochord (nc) (**a, a'**), or that differentiated in a muscle fiber at the somite ventral border (**b, b'**). Scale bars, 10 μ m. **E** Histogram showing the percentage of each cell type differentiated at 48 hpf from single cells photoconverted at 23 hpf. Forty-two cells were analyzed from three independent experiments. **F** (**a**) Schematic representation of the developmental fates of photoconverted sclerotome cells; **b** localization of each derivative after migration. DMC dorsal mesenchymal cell, SC stromal cell, MF muscle fiber, FMC fin mesenchymal cell, NC notochord, NT neural tube, CA caudal artery, CV caudal vein, Som somite.

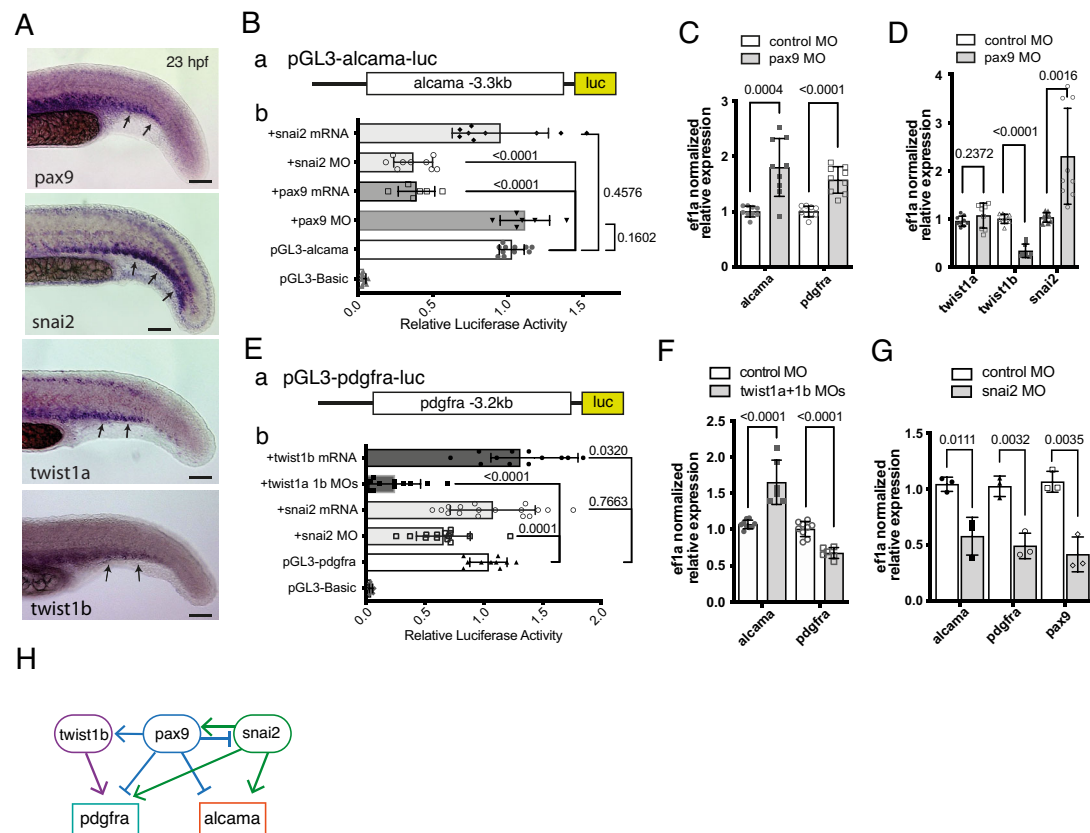


Fig. 6 | *alcama* and *pdgfra* are regulated by sclerotome-associated TFs. **A** WISH for *pax9*, *snai2*, *twist1a*, and *twist1b* at 23 hpf in the tail of WT embryos. Arrows point to expression of these genes in the somitic VCs. **B** (a) a DNA fragment encompassing 3.3 kb upstream of the *alcama* gene transcription start site was inserted upstream of the luciferase (luc) coding region of the pGL3-Basic plasmid, to give pGL3-*alcama*-luc. **b** In situ luciferase assays at 23 hpf following pGL3-*alcama*-luc injection at the 1-cell stage either alone or together with the indicated mRNA or MO; each lysate was obtained from 10 to 15 tails ($n = 9$ lysates for each condition, as biological triplicates from three independent experiments) or *pax9* ($n = 6$ for each). The pGL3-Basic and pGL3-*alcama*-luc ($n = 11$ for each) were used as negative and positive controls, respectively (mean \pm SD; one-way ANOVA followed by Dunnett's multiple comparison test). **C** qPCR analysis for *alcama* and *pdgfra* in *pax9* morphants and control ($n = 9$ pooled tail samples for each, a set of biological triplicates from three independent experiments) at 23 hpf. Mean \pm SD; two-tailed Student's *t*-test. **D** qPCR analysis for *twist1a*, *twist1b*, and *snai2* in *pax9* morphants and control ($n = 9$ pooled tail samples for each, measured examined over three

independent experiments) at 23 hpf. mean \pm SD; two-tailed Student's *t*-test. **E** (a) a DNA fragment covering 3.2 kb upstream of the *pdgfra* gene transcription start site was inserted upstream of the luciferase (luc) coding region to give pGL3-*pdgfra*-luc. **b** Same experimental scheme as in **B-b**, following injection of the indicated constructs and MO or mRNA combinations ($n = 12, 11, 17$, and 14 lysates for *twist1b* mRNA, *twist1a* 1b MOs, *snai2* mRNA and *snai2* MO examined over three independent experiments). mean \pm SD; One-way ANOVA followed by Dunnett's multiple comparison test. **F** qPCR analysis for *alcama* and *pdgfra* ($n = 6$ pooled tail samples for each, measured examined over two independent experiments) in *twist1a*/*twist1b* double morphants and control at 23 hpf. Mean \pm SD; two-tailed Student's *t*-test. **G** qPCR analysis for *alcama*, *pdgfra*, and *pax9* in *snai2* morphants and control ($n = 3$) at 23 hpf (mean \pm SD; two-tailed Student's *t*-test). **H** Proposed network of TFs acting on *alcama* and *pdgfra* during SCP development; lines ending with arrow or bar represent activation or repression, respectively. Source data for **B-G** are provided as a Source Data file.

(Fig. 7B, C-a, D-a; Supplementary Movie 8). Time-lapse confocal imaging showed their dynamics in the sub-aortic space (Supplementary Movie 9). As in the caudal region, we found that *Alcama*, *Pdgfr- α* or *Pax9* deficiency led to a strong reduction of these *pax3a:eGFP⁺* or *ET37:eGFP⁺* stromal cells of the trunk (Fig. 7C, D). In addition, these cells were found lateral or ventro-lateral to the aorta, but never just ventral to it (Fig. 7C, D). By 52 hpf, the same defects in their positioning were still observed (Supplementary Figs. 6Aa-d, Ba-d), and their total number in the trunk was even more reduced relative to control embryos than at 36 hpf (Supplementary Figs. 6A-e, B-e).

Totally, 36 hpf is the developmental stage by which definitive HSPCs begin to emerge by EHT from the ventral wall of the aorta—a process that peaks by 48–52 hpf⁴. We found that *Alcama*, *Pdgfr- α* , or *Pax9* deficiency all caused a dramatic reduction in *myb⁺* HSPCs in the trunk by 36 hpf (Fig. 7E, F). At the same time point, we could observe the beginning of *myb⁺* HSPC colonization of the CHT of control embryos, whereas almost no *myb⁺* cell was detected in the CHT of all morphants (Fig. 7E-a). Then, at 52 hpf, only few *myb⁺* HSPCs were found in the trunk of all morphants, even less than at 36 hpf, while

myb⁺ cells were numerous in control embryos, and very few *myb⁺* HSPCs were detected in the CHT of all morphants (Fig. 7E-b). Thus the severe impact of *Alcama* or *Pdgfr- α* deficiency on the development of sclerotome-derived stromal cells both in the trunk (Supplementary Fig. 6C) and in the tail altogether led to profoundly defective definitive hematopoiesis.

Discussion

Mouse studies have shown the presence of various stromal cell subsets in hematopoietic stem cell niches⁸. However, the developmental process and behavior of these cells, and the molecules involved in cell-cell interactions during niche formation, remain a mystery. In the present study, we have taken advantage of the accessibility to in vivo observations of the zebrafish CHT, the hematopoietic homolog of the fetal liver niche in mammals, to provide new insights into the genesis of stromal cells. We previously found that the stromal cells of the CHT arose from ventral clusters (VCs) within the caudal somites. We report here a new transgenic line, *TgBAC(cspg4:Gal4)*, that specifically labels these VCs and their derivatives, notably the SCPs throughout their

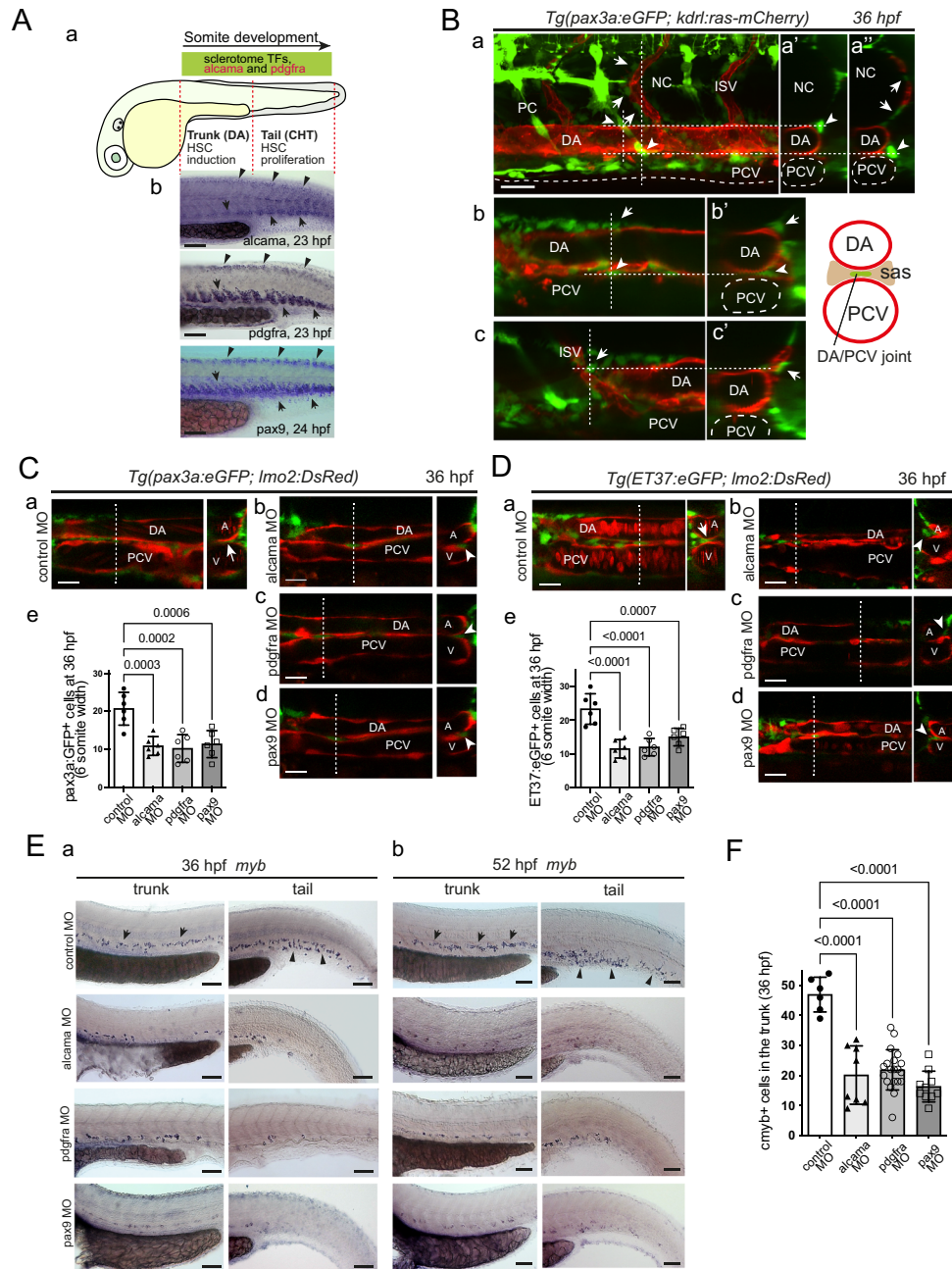


Fig. 7 | Alcama and Pdgfr- α are also involved in stromal cell development in the trunk, which conditions the development of definitive HSPCs. A (a) Rostro-caudal extent of sclerotomal TFs and *alcama* and *pdgfra* expression by 24 hpf. **b** WISH for *alcama*, *pdgfra*, and *pax9* at 23–24 hpf. Arrows point at their expression in the somite VCs/sclerotome in the trunk and tail. Arrowheads point at their expression in the smaller dorsal sclerotome¹⁵. **B** Confocal maximum projection (**a**) and single confocal sections (**b, c**) of the trunk region of a *Tg(pax3a:eGFP; kdr1:ras-mCherry)* embryo at 36 hpf, with vertical dashed lines showing the position of the optical transverse sections shown on the right (**a'**, **a''**, **b'**, **c'**). Arrowheads point at GFP⁺ stromal cells located at the DA/notochord or DA/PCV junction, arrows point at ISV-associated mesenchymal cells, known to originate from the dorsal-wards migration of ventral sclerotome cells^{12,15}. Scale bar, 20 μ m. **C, D** Confocal sections of the trunk region of *Tg(pax3a:eGFP; lmo2:DsRed)* (**C**) and *Tg(ET37:eGFP; lmo2:DsRed)* (**D**) embryos injected with control (**a**), *alcama* (**b**), *pdgfra* (**c**), or *pax9* (**d**) MOs. Dashed lines indicate the position of the corresponding transverse section shown on the right. Arrows and arrowheads point at stromal cells located at the DA/PCV

joint or somewhat lateral to it, respectively. **e** Quantification of *pax3a:eGFP*⁺ (**C**) or *ET37:eGFP*⁺ (**D**) cells in the sub-aortic space of 36 hpf live embryos injected with control, *alcama*, *pdgfra* or *pax9* MO (mean \pm SD; *n* = 6 embryos for each group. One-way ANOVA followed by Dunnett's multiple comparison test). Counting was done over a 6-somite width. Scale bars, 20 μ m. **E** WISH for *myb* at 36 (**a**) and 52 (**b**) hpf in embryos injected with control, *alcama*, *pdgfra*, or *pax9* MO. Arrows and arrowheads point at *myb*⁺ signals in the trunk (arrows) and tail (arrowheads) regions, respectively. **a** Representative images of *n* = 6, 8, 20, and 10 injected embryos for control, *alcama*, *pdgfra*, and *pax9* MO, respectively, from two independent experiments. **b** Representative images of *n* = 6 for each condition, from two independent experiments. Scale bars, 100 μ m. **F** Quantification of *myb*⁺ cells at 36 hpf as shown in (**E-a**) (mean \pm SD; *n* = 6 embryos for control, 8 for *alcama*, 20 for *pdgfra*, and 10 for *pax9* MO-injected embryos. One-way ANOVA followed by Dunnett's multiple comparison test). DA or A dorsal aorta, PCV or V posterior cardinal vein, ISV intersomitic vessel, sas sub-aortic space. Source data for **C-e**, **D-e**, and **F** are provided as a Source Data file.

development, and at least two other types of mesenchymal cells—dorsal-wards migrating cells (DMCs) and fin mesenchymal cells (FMCs)³⁵.

VC cells specifically express sclerotome marker genes such as *nkx3.1*, *pax9*, *twist1a/b*, and *snai2*. We found via double WISH and in vivo tracking of sclerotomal cells from the caudal somites that the VCs indeed coincide with the sclerotome. Historically the sclerotome has been defined as the ventro-medial layer of the early, still epithelial somites that become mesenchymal cells via an EMT, and then migrate to encircle the notochord and differentiate into chondro- and osteogenic derivatives to form the vertebrae. Later it was found to also give rise to other migrating mesenchymal cells that would become mural cells (pericytes and vascular smooth muscle cells-vSMCs) ensheathing the dorsal artery and other vessels, both in amniotes¹¹ and more recently in zebrafish^{12,13,14} as well as tenocytes (tendon cells) attaching somite muscle fibers to the bones¹⁵, and perivascular fibroblasts¹²—a cell population that would likely later also give rise to adipocytes⁴³. To these sclerotomal derivatives we are now adding, for the caudal region, the stromal cells of the CHT, and the mesenchymal cells of the ventral side of the caudal fin (FMCs, that will become fibroblasts in the adult fin³⁵), as similarly found by Ma et al.¹⁵ for the dorsal side of the caudal fin. Considering that the cell population originating from the caudal somites that differentiate into osteoblasts in adult fish⁴⁴ may also be included, cells from the VCs/sclerotome may be considered as multipotent mesenchymal progenitors, with a range of fates wider than the threefold (chondro-, osteo-, and adipo-genic) potential usually assayed in vitro to assert the Mesenchymal Stem Cell (MSC) capability of cells isolated from various neonatal or adult tissues in mammals⁴⁵. Strikingly, the three transmembrane molecules that we found here to be more specifically expressed in the VCs and their derivatives, Alcama, Pdgfr- α , and Cspg4 (also known as NG2), have all been used in mammals as markers of bone marrow and/or fetal liver mesenchymal stromal cells to purify these cells, that were then often shown to be endowed with MSC capability in vitro^{8,23,32,33,46}. This further suggests to us that like the stromal cells of the zebrafish CHT, stromal cells of mammalian hematopoietic niches in the trunk and limbs may have a sclerotomal origin and that Alcama and Pdgfr- α will no longer be seen as mere markers of these cells, but as essential for their ontogeny.

It will be important to determine when and how the “commitment” process⁴⁷, which corresponds to the first branching point in the differentiation of multipotent mesenchymal cells into various cell lineages, may take place within the sclerotome. Our tracking of caudal sclerotome-derived cells presently suggests that their fate within the VCs may already be restricted by somite maturation stage S8. The development of genetic tools to mark the sclerotome earlier will be needed to conclude on this point.

We further found that Alcama-, Pdgfr- α -, and Pax9-dependent, hence sclerotome-derived pax3a:eGFP⁺/ET37:EGFP⁺ cells are present not only in the tail but also in the trunk, as mesenchymal cells associated with the DA and underlying axial vein (PCV), and that they foster the emergence of HSPCs from the DA. Nguyen et al.⁴⁸ previously found somite-derived pax3a:GFP⁺ cells that fostered HSPC emergence, and they interpreted them as partly endothelial cells (of the DA and other vessels) and partly “vascular associated cells” (“VACs”). In our own analysis, we found all pax3a:GFP⁺ cells to be VACs, part of them in very close apposition to the DA or PCV endothelium, highly reminiscent of the stromal mesenchymal cells that we had previously imaged at that same position and developmental stages by electron microscopy⁶. These cells most likely include precursors of the mural cells (vSMCs and pericytes), known to derive from the sclerotome^{12,14}. Studies by Traver and colleagues^{49,50} found that HSPC ontogeny required somitic Wn16-induced Dlc/Dld signaling to angioblasts by 15–17 hpf during their migration towards the midline along the ventral surface of somites, where the early sclerotome lies. Therefore the sclerotome may possibly foster HSPC emergence at two successive stages, first

through such direct contact with and signaling to migrate DA precursors, and later through the interaction of sclerotome-derived mesenchymal cells with the DA hemogenic endothelium.

Thus the sclerotome successively gives rise to mesenchymal cells involved in the first two main stages of HSPC development and function. Trunk somites first contribute mesenchymal stromal cells that foster the emergence of HSPCs from the DA floor, then also likely facilitate their intravasation into the circulation through the dorsal wall of the underlying PCV. We indeed previously found by electron microscopy stromal mesenchymal cells bridging gaps between endothelial cells of the PCV dorsal wall through which we had shown that aorta-derived HSPCs enter blood circulation⁶. Then the later formed caudal somites contribute stromal cells that are key components of the niche where the aorta-derived HSPCs will first settle, expand and undergo multi-lineage differentiation. We found that Alcama and Pdgfr- α expression in the sclerotomal compartments of the trunk and tail are both necessary to give rise to these two sets of mesenchymal stromal cells that are successively essential for the development of definitive hematopoiesis. In addition, they appear similarly involved in the generation of mesenchymal cells of the caudal fin from both the ventral and dorsal sclerotome compartments.

We identified the earliest morphological individualization of the caudal sclerotome as a distinct ventral cell cluster appearing at somite maturation stage S5 (in agreement with Morin-Kensicki et al.⁹ for the trunk somites) and encompassing the whole mediolateral extent of the somite before these cells become mesenchymal and migrate both dorsal- and ventral-wards. Interestingly, Naganathan et al.⁵¹ recently found that the antero-posterior length of freshly formed somites is somewhat variable and that over the next 1–2 h (i.e., until somite stage S4), they undergo a mechanical adjustment of this A–P length that is facilitated by somite surface tension, which requires the somite to be fully packed within an uninterrupted basal lamina. It, therefore, makes sense that cell migrations out of the somite, which require breaking the basal lamina, can be “allowed” to begin only once this mechanical rearrangement of the somite has been completed, i.e. from somite stage S4/S5.

Morphological individualization of VCs by somite stage S5 as a 3D ‘rosetta’ with a small central lumen appears concomitant with the onset of expression at the same place of the TF genes *twist1a/b* and *pax9*, which may thus trigger the EMT, and of *pdgfra*. Since *alcama* and *snai2* transcripts are already detected at the somite ventral and dorsal borders by stage S1/S2 (Figs. 1C and 6A), our data of Fig. 6B–G suggest that Snai2 may be sufficient to activate *alcama* transcription at stages S2–S4, whereas Twist1b may be additionally required for the activation of *pdgfra* transcription as well as for the EMT by stage S5 (Supplementary Fig. 7).

Unlike *alcama* transcripts, the Alcama protein first appears in the center of the cluster by stage S5 and then gradually spreads to all interfaces among cluster cells. Then as these cells emigrate from the cluster, they do so as strings of cells still enriched in Alcama at their interfaces. Suppression of Alcama function reduced the number of emigrating SCPs, their contacts among each other, and their migratory capacity. The latter defect correlated with a less efficient polarization of the cell and its F-actin dynamics relative to the ventral direction of migration. When ventral cluster cells overexpressed a mutant Alcama deleted of its two N-terminal Ig domains (that mediate homophilic cell-cell adhesion), they started displaying extreme filopodial dynamics while still within the clusters. This may be favored by the lack of Alcama-mediated cell-cell contacts, while the still present short ICD of this overexpressed Δ N-Alcama form may trigger more F-actin dynamics generating filopodia. Conversely, ventral cluster cells overexpressing a mutant Alcama form in which the ICD is no longer able to bind PDZ domain-containing actin-binding proteins such as syntenin-1^{26–28} showed a lack of filopodial dynamics, more extended cell-cell contacts, and an even more complete lack of apparent cell polarity.

This phenotype could be related to the fact that when the link of transmembrane Alcama molecules to the cytoskeleton is suppressed, they are freer to cluster within the membrane, which in turn reinforces Alcama-mediated cell–cell contacts⁵².

Suppression of Pdgfr- α function affected the emergence and ventral-wards migration of SCPs at least as strongly as Alcama deficiency, whereas neither affected the dorsal-wards migration of DMCs. Our finding that both Alcama and Pdgfr- α deficiencies led to a strong decrease in pERK signaling in the ventro-caudal region suggests that the intracellular signaling pathways downstream of Alcama and Pdgfr- α overlap within the SCPs. In addition, we found PI3K activation to be an obligatory step downstream of Pdgfr- α activation for the development of these cells. Interestingly, the dorsal-wards migration of sclerotome cells was also affected in embryos treated with a PI3K α inhibitor, indicating that even though distinct pathways are likely involved in the dorsal and ventral migrations of sclerotome derivatives, both use PI3K as a necessary downstream effector (Supplementary Fig. 7).

Our new *Tg(cspg4:Gal4)* line, which highlights these cells from their sclerotomal origin onwards, will be a precious tool to discern, notably through single-cell transcriptome analysis, whether cellular heterogeneities prefiguring different fates are already present within the somitic VCs and how different the stromal cells fostering HSPC emergence from the aorta are from those that then nurture HSPC expansion and multi-lineage differentiation in the CHT niche. Elucidation of the molecular mechanisms of cell commitment within the multipotent sclerotome should contribute to the field of regenerative medicine by facilitating the induction and manipulation of rare MSC populations from adult tissues.

Methods

Zebrafish

Fish were maintained in our zebrafish facility at Institut Pasteur. Embryos were obtained through natural crosses, raised at 28 °C in embryo water [Volvic® water containing 0.28 mg/ml Methylene Blue (M-4159; Sigma) and 0.03 mg/ml 1-phenyl-2-thiourea (P-7629; Sigma)], and staged according to Kimmel et al.⁵³ For this study, we used the previously described transgenic lines *Tg(ET37:EGFP)*⁵⁴, *Tg(pax3a:EGFP)*^{iso 55}, *Tg(UAS:Lifect-GFP)*^{mu271 36}, *Tg(7xTCF-Xla.Siam.nlsMCherry)*⁵⁶, *Tg(kdrl:rasMCherry)*⁵⁷, *Tg(lmo2:DsRed)*⁵⁸ and *Tg(ola-twist:Gal4; UAS:Kaede)*³⁵.

BAC recombineering and transgenesis

The tol2 and BAC recombineering vectors were kindly provided by K. Kawakami (National Institute of Genetics, Mishima). A BAC DNA containing the *cspg4* gene (DKEY-105I23) was purchased from Source BioScience. The *TgBAC(cspg4:Gal4)* line was firstly generated by recombining a iTol2-amp cassette to the BAC vector⁵⁹, then a second recombineering was performed targeting a cassette containing GAL4 (pGAL4FF-FRT-Kan-FRT) flanked by 50 bp arms homologous to the region around the translation start of the *cspg4* gene. Primers used for the 1st and 2nd recombineering steps are listed in Supplementary Table 1). Recombination was performed using RedET methodology (K001, GeneBridges) as described in a previous report⁶⁰. BAC DNAs were prepared using NucleoBond BAC 100 (740579, Marchery-Nagel). *Tg(UAS:RFP)* embryos were injected with 1 nl of mixed solution of 100 ng/ μ l BAC DNA and 50 ng/ μ l Tol2 mRNA at the 1-cell stage.

In situ hybridization, immunostaining, and Western blotting

Whole-mount RNA in situ hybridization (WISH) was performed according to Thisse (<https://wiki.zfin.org/display/prot/Thisse+Lab+-+In+Situ+Hybridization+Protocol+-+2010+update>). Riboprobes were synthesized by reverse transcription from PCR fragments amplified from cDNA synthesized from the tails of WT embryos as templates, or from linearized plasmids. The probes used in this study are indicated in Supplementary Tables 2a and 2b.

Double WISH was performed with the following modifications to the above protocol. Riboprobes were synthesized using Digoxigenin-11-UTP or Fluorescein-12-UTP (Roche) then signal detection was performed by horseradish peroxidase (POD)-based method followed by tyramide-based signal amplification (TSA)⁶¹. To increase the sensitivity of probe detection containing Fluorescein-12-UTP, the probe was first reacted with an anti-Fluorescein-R-phycoerythrin antibody (Invitrogen, A21250, 1/100) followed by an anti-rabbit-POD secondary antibody (Sigma, A0545, 1/200).

Whole-mount fluorescent immunostaining was carried out as described⁵. The list of primary and secondary antibodies and concentrations used is shown in Supplementary Table 3.

For the Western blotting, tails at 24 hpf were solubilized on ice in lysis buffer (50 mM Tris-HCl, 150 mM NaCl, 2.5 mM EDTA, 1% Triton X100, 1X final protease inhibitors cocktail, pH 8) at a ratio of 20 tails/20 μ l. After 30 min solubilization on ice, samples were centrifuged at 4 °C for 10 min at 13,000 rpm. Supernatants were transferred to new tubes and aliquots of the samples were treated for protein determination using BCA reagents (Sigma) with BSA standards ranging from 62.5 to 250 mg/ml. Samples were then adjusted for loading 67.5 μ g per well of total protein. After SDS-PAGE (12% acrylamide gels), proteins were transferred onto nitrocellulose (Protran, 0.45 μ m) using a Genie Blotter system (Idea Scientific Company). Membranes were then incubated for 60 min in blocking buffer (Tris Buffered Saline (TBS) complemented with 0.1% tween-20 (TBST) and 5% w/v low-fat milk). Anti-Alcama monoclonal antibodies (Zn-8, Developmental Studies Hybridoma Bank) were diluted in blocking buffer (1/2000) and incubated with membranes overnight, at 4 °C. After extensive washing in TBST, membranes were incubated with peroxidase-coupled anti-mouse antibodies diluted in TBST for 2 h at room temperature. Complexes were revealed via chemiluminescence using ECL Prime western blotting detection reagents (ThermoFisher Scientific) and the Bio-Rad Chemidoc MP imaging system.

Construction of mutant forms of Alcama and Pdgfra, transient transgenesis, and heat-shock treatment

UAS:alcama- Δ N-eGFP, UAS:alcama- Δ PDZ-eGFP and UAS:alcama-FL-eGFP. We first cloned the *alcama* ORF to utilize it as a template for the following PCRs (details of cloning are indicated below). For *alcama- Δ N* construct, a DNA fragment missing to encode amino acids 25–238 corresponding to the two amino-terminal Ig-like domains of Alcama was amplified. For the *alcama- Δ PDZ* construct, 3 amino acid substitutions were introduced in a putative PDZ domain binding motif at positions 533–539 (KTRQGSW->MVRQGS) by site-directed mutagenesis. Primers used for the mutagenesis are listed in Supplementary Table 4. Control *alcama-FL* (full length) and mutated *alcama* fragments were cloned into the Nco I site of UAS:eGFP vector in frame with eGFP using Gibson assembly (#E5510, NEB).

hsp70:pdgfra- Δ PI3K-HA and hsp70:pdgfra^{WT}-HA. A zebrafish *pdgfra- Δ PI3K* was designed based precisely on a human dominant-negative *pdgfra*, with the substitutions Y706F (Y731F in humans) and Y717F (Y742F)²⁹. Fragments containing amino acid substitutions were amplified by PCR using the clone containing full-length WT *pdgfra* (kindly provided by J. Eberhart, University of Texas at Austin) as a template. A 3 kb fragment covering the ORF was amplified in three fragments and the point mutations were introduced in the appropriate fragments using primers listed in Supplementary Table 4. A tandem HA-tag sequence was added in the frame at the C-terminus of *pdgfra*. Fragments encoding control or mutant *pdgfra* were cloned into hsp70 vector using Gibson assembly.

Plasmid DNA for each construct was co-injected with capped mRNA coding for the Tol2 transposase into 1-cell stage embryos at the amount of 250 and 25 pg, respectively. Embryos were heat-shocked by

placing them in pre-warmed Volvic water for 30 min at 39 °C then transferred to 28 °C until in vivo observation.

RNA/cDNA synthesis, plasmid construction, and injection

Total RNA was extracted with the TRIzol reagent (15596026, Invitrogen) from tails of anesthetized embryos at 23 hpf. Tail total RNA was reverse transcribed into cDNA using a Superscript IV reverse transcriptase (18091050, Invitrogen). For *alcama*, *pdgfaa*, *pdgfab*, *pdgffb*, and *twist1b*, ORFs were amplified by PCR using tail cDNA as a template for the subcloning into the TOPO vector and then reinserted into pExpress1 vector using Gibson assembly. ORFs of *pax9* and *snai2* were amplified by PCR from tail cDNA then cloned directly into pExpress1 vector. Primers used for the cloning are listed in Supplementary Table 5. mRNAs were synthesized using mMessage mMachinE transcription kit (AM1344, Ambion). Capped mRNAs were injected into 1-cell stage embryos at the amount of 100 pg.

Morpholinos and qPCR

Morpholino oligonucleotides (Gene Tools) were injected (0.5–1 nl) into the 1-cell-stage embryo at the amount specified; *alcama* MO²⁰ (2 ng), *pdgfra* MO⁴⁰ (4 ng), *pax9* MO^{62,63} (6 ng), *snai2* MO^{63,64} (8 ng), and *twist1a* and *twist1b* MOs⁶⁵ (2 ng each). MO sequences are shown in Supplementary Table 6. For quantitative real-time PCR (qPCR), total RNA was extracted from 3 independent groups of 40 tails dissected from embryos at 23 hpf to synthesize template cDNAs. The primers used for qPCR are shown in Supplementary Table 7. All qPCR experiments were performed with measurements taken from 3 technical replicates. Fold changes in gene expression were calculated using the $2^{-\Delta\Delta CT}$ method and normalized to *e1a*.

Promoter cloning and Dual-Luciferase assay

3.3 and 3.2 kb promoter regions of *alcama* and *pdgfra* genes were cloned from BAC DNA (*alcama*: RP71-78P1, BACPAC Resources; *pdgfra*: DKEY-97C6, Source BioScience) and cloned into the pGL3 basic vector (E1751, Promega) linearized with Xho I and Hind III (pGL-*alcama*-luc and pGL-*pdgfra*-luc). Primers used for promoter cloning are listed in Supplementary Table 8. To assess *alcama* and *pdgfra* promoter activities in response to various TFs, WT embryos were injected at the 1-cell stage with luciferase vectors (pGL-*alcama*-luc or pGL-*pdgfra*-luc), control (Renilla) expression vector (pRL-TK; E2241, Promega), and a specified amount of Morpholino or appropriate mRNA encoding TF (co-injection condition is listed in Supplementary Table 9). Ten to fifteen tails were dissected from the injected embryos at 23–24 hpf and lysed with passive lysis buffer (E1941, Promega) for subsequent Dual-Luciferase assay following the manufacturer's instructions (E1910, Promega).

Drug treatments

Pharmacological inhibitors were all solubilized in DMSO (Sigma) and appropriate DMSO controls (0.2%) were used for all experiments. Embryos treated with AS605240 (2 μM; S1410, Selleckchem), LY294002 (20 μM; S1105, Selleckchem), and CAL101 (10 μM; S2226, Selleckchem) from 19–20 hpf embryos then live-images were taken with drugs in agarose and embryo water supplemented with tricaine. For WISH, embryos were treated with a drug from 19 to 20 hpf until the stage of interest, then fixed in 4% methanol-free formaldehyde overnight.

Generation of *alcama* and *pdgfra*-crispants

Transient CRISPR-Cas9 targeting of the *alcama* and *pdgfra* genes was performed by using Alt-R CRISPR-Cas9 system (Integrated DNA Technologies / IDT). The gRNA target sites (shown in Supplementary Table 10) were evaluated for the off-target sites by using the sgRNA design tool (IDT). Alt-R S.p. Cas9 V3 enzyme (IDT) and equimolar amount of crRNA:tracrRNA duplexes (IDT) were mixed and incubated

to form RNP complexes before injection. The mixed solution was diluted with Cas9 buffer (NEB) to adjust the concentration of Cas9 and sgRNA working solution to 12 and 18 μM, and 1 nl was injected into the cytoplasm of one-cell stage *Tg(pax3a:eGFP; kdrl:ras-mCherry)* embryos. Injected F0 crispant embryos were individually screened by genomic PCR using primers that recognize outer sites of the region sandwiched by a pair of gRNA (for *alcama*) or primers designed at intron2/exon3 of the *pdgfra* gene. For the cDNA analysis of *pdgfra*-crispants, total RNA was extracted from 100 to 120 pooled embryos and RT-PCR was performed using primers designed at exon2/exon4 to check the resulting splicing patterns. The primers used are shown in Supplementary Table 10.

Live imaging, image processing, and quantification

VE-DIC (video-enhanced differential interference contrast) microscopy was performed using a Polyvar2 microscope (Reichert) as described previously⁶⁶. Confocal fluorescence microscopy was performed on Leica SPE and SP8 set-ups and Andor spinning disk set-ups as described previously^{4,7}. Image processing was basically performed using Fiji⁶⁷. Measurements of surface area and volume on migrating SCPs were performed using IMARIS software (Bitplane). Cell tracking was performed using a Manual tracking plugin (Fiji) and the obtained data were (1) plotted with a Python script developed by S. Rigaud (Image Analysis Hub (IAH) of Institut Pasteur) or (2) imported into the Chemotaxis and Migration Tool plugin⁶⁸ (Fiji). For the analysis of filopodial dynamics, Filopodyan plugin⁶⁹ was used in Fiji. First, we obtained a time-lapse movie (6 min intervals, 23–38 hpf) of the migrating lifeact-GFP⁺ SCPs injected with control or *alcama* MO (7 leader cells were analyzed for each condition). We extracted 7–10 timepoints from the time that the leader cell left its followers and measured the orientation of the filopodia for each timepoint. The cut-off threshold was set to 3 μm. The direction of SCP migration was obtained from the positional information at the first and last timepoints. The angle of filopodia relative to the direction of SCP migration was calculated with a Python script developed by D. Ershov (IAH, Institut Pasteur). Photoshop and Illustrator (Adobe) were used to combine two or more confocal images to display a wide view (joints are indicated by dotted lines in each figure).

Single-cell photoconversion and confocal imaging

Photoconversion was achieved using an Andor (Oxford Instruments) spinning disk confocal system (CSU-W1 Dual camera with 50 μm disk pattern and single laser input (445/488/561/642 nm), LD Quad 405/488/561/640 and triple 445/561/640 dichroic mirrors), equipped with a Leica DMI8 fluorescence inverted microscope, a Digital Mirror Device (DMD-Mosaic 3 (Andor)), and CMOS cameras (Orca Flash 4.0 V2 + (Hamamatsu)). *Tg(ola-twist:Gal4; UAS:Kaede)* embryos were kept in the dark at 28 °C until 23 hpf then mounted in 1% low-melting agarose. Photoconversion of the Kaede in single cells at the ventral side of caudal somites S8-S11 at 23 hpf was performed at 408 nm, using a 63x water immersion objective (HC PL APO 63x/1.20 W CORR CS2), a LEDs light source (CoolLED pE-4000 16 wavelength LED fluorescence system), and the DMD-Mosaic-3 with the support of the MetaMorph software. After photoconversion, embryos were kept mounted at 28 °C for 1 h and subsequently time-lapse imaged at 6 min intervals using a Leica SP8 confocal microscope as described above.

Statistics and reproducibility

Statistical analysis was performed using GraphPad Prism 9. For data that followed a normal distribution analyzed by the Shapiro–Wilk test, statistical significance was assessed by a two-tailed Student's *t*-test, while Mann–Whitney test was introduced for two groups with unequal variances. One-way ANOVA was performed to analyze the differences among multiple groups, followed by Tukey's or Dunnett's multiple comparison test. Data are shown as mean or median ± SD. For the

calculation of exact p values below $p < 0.0001$ for t -tests, the t -score and degrees of freedom (DF) values were added to the source data. For ANOVA, SS (sums of squares), MS (mean square), DF and F distribution were also added to the appropriate source data. For confocal analysis for Tg embryos, expression patterns were confirmed in at least 6 independent animals. All WISH patterns were confirmed in at least 6 independent animals. In vivo observations of non-treated wild-type embryos were performed at least five times, and WISH and IHC were basically performed at least three times unless stated otherwise. For qPCR and luciferase assays, results were collected with three biological replicates.

Reporting summary

Further information on research design is available in the Nature Portfolio Reporting Summary linked to this article.

Data availability

Raw imaging files are available upon request due to their large size. Source data are provided in this paper.

Code availability

All software and plug-ins used in this study are either freely or commercially available.

References

- Kissa, K. & Herbolme, P. Blood stem cells emerge from aortic endothelium by a novel type of cell transition. *Nature* **464**, 112–115 (2010).
- Bertrand, J. Y. et al. Haematopoietic stem cells derive directly from aortic endothelium during development. *Nature* **464**, 108–111 (2010).
- Boisset, J. C. et al. In vivo imaging of haematopoietic cells emerging from the mouse aortic endothelium. *Nature* **464**, 116–120 (2010).
- Lancino, M. et al. Anisotropic organization of circumferential actomyosin characterizes hematopoietic stem cells emergence in the zebrafish. *Elife* **7**, e37355 (2018).
- Murayama, E. et al. Tracing hematopoietic precursor migration to successive hematopoietic organs during zebrafish development. *Immunity* **25**, 963–975 (2006).
- Kissa, K. et al. Live imaging of emerging hematopoietic stem cells and early thymus colonization. *Blood* **111**, 1147–1156 (2008).
- Murayama, E. et al. NACA deficiency reveals the crucial role of somite-derived stromal cells in haematopoietic niche formation. *Nat. Commun.* **6**, 8375 (2015).
- Wei, Q. & Frenette, P. S. Niches for hematopoietic stem cells and their progeny. *Immunity* **48**, 632–648 (2018).
- MorinKensicki, E. M. & Eisen, J. S. Sclerotome development and peripheral nervous system segmentation in embryonic zebrafish. *Development* **124**, 159–167 (1997).
- Stickney, H. L., Barresi, M. J. F. & Devoto, S. H. Somite development in zebrafish. *Dev. Dyn.* **219**, 287–303 (2000).
- Pouget, C., Gautier, R., Teillet, M. A. & Jaffredo, T. Somite-derived cells replace ventral aortic hemangioblasts and provide aortic smooth muscle cells of the trunk. *Development* **133**, 1013–1022 (2006).
- Rajan, A. M., Ma, R. C., Kocha, K. M., Zhang, D. J. & Huang, P. Dual function of perivascular fibroblasts in vascular stabilization in zebrafish. *PLoS Genet.* **16**, e1008800 (2020).
- Ando, K. et al. Clarification of mural cell coverage of vascular endothelial cells by live imaging of zebrafish. *Development* **143**, 1328–1339 (2016).
- Stratman, A. N. et al. Interactions between mural cells and endothelial cells stabilize the developing zebrafish dorsal aorta. *Development* **144**, 115–127 (2017).
- Ma, R. C., Jacobs, C. T., Sharma, P., Kocha, K. M. & Huang, P. Stereotypic generation of axial tenocytes from bipartite sclerotome domains in zebrafish. *PLoS Genet.* **14**, e1007775 (2018).
- Degen, W. G. J. et al. MEMD, a new cell adhesion molecule in metastasizing human melanoma cell lines, is identical to ALCAM (activated leukocyte cell adhesion molecule). *Am. J. Pathol.* **152**, 805–813 (1998).
- Patel, D. D. et al. Identification and characterization of a 100-kD ligand for CD6 on human thymic epithelial cells. *J. Exp. Med.* **181**, 1563–1568 (1995).
- Ferragut, F., Vachetta, V. S., Troncoso, M. F., Rabinovich, G. A. & Elola, M. T. ALCAM/CD166: a pleiotropic mediator of cell adhesion, stemness and cancer progression. *Cytokine Growth Factor Rev.* **61**, 27–37 (2021).
- Bye, C. R., Rytova, V., Alsanie, W. F., Parish, C. L. & Thompson, L. H. Axonal growth of midbrain dopamine neurons is modulated by the cell adhesion molecule ALCAM through trans-heterophilic interactions with *l1cam*, *Chl1*, and semaphorins. *J. Neurosci.* **39**, 6656–6667 (2019).
- Choe, C. P. et al. Wnt-dependent epithelial transitions drive pharyngeal pouch formation. *Dev. Cell* **24**, 296–309 (2013).
- Cizelsky, W., Tata, A., Kuhl, M. & Kuhl, S. J. The Wnt/JNK signaling target gene *alcam* is required for embryonic kidney development. *Development* **141**, 2064–2074 (2014).
- Willrodt, A. H. et al. Stromal expression of activated leukocyte cell adhesion molecule promotes lung tumor growth and metastasis. *Am. J. Pathol.* **187**, 2558–2569 (2017).
- Arai, F., Ohneda, O., Miyamoto, T., Zhang, X. Q. & Suda, T. Mesenchymal stem cells in perichondrium express activated leukocyte cell adhesion molecule and participate in bone marrow formation. *J. Exp. Med.* **195**, 1549–1563 (2002).
- Brinkhof, B., Zhang, B., Cui, Z., Ye, H. & Wang, H. ALCAM (CD166) as a gene expression marker for human mesenchymal stromal cell characterisation. *Gene* **763S**, 100031 (2020).
- Anker, P. S. et al. Mesenchymal stem cells in human second-trimester bone marrow, liver, lung, and spleen exhibit a similar immunophenotype but a heterogeneous multilineage differentiation potential. *Haematologica* **88**, 845–852 (2003).
- Tudor, C. et al. Syntenin-1 and Ezrin proteins link activated leukocyte cell adhesion molecule to the actin cytoskeleton. *J. Biol. Chem.* **289**, 13445–13460 (2014).
- te Riet, J. et al. Dynamic coupling of ALCAM to the actin cortex strengthens cell adhesion to CD6. *J. Cell Sci.* **127**, 1595–1606 (2014).
- te Riet, J. et al. Distinct kinetic and mechanical properties govern ALCAM-mediated interactions as shown by single-molecule force spectroscopy. *J. Cell Sci.* **120**, 3965–3976 (2007).
- Rosenkranz, S., DeMali, K. A., Gelderloos, J. A., Bazenet, C. & Kazlauskas, A. Identification of the receptor-associated signaling enzymes that are required for platelet-derived growth factor-AA-dependent chemotaxis and DNA synthesis. *J. Biol. Chem.* **274**, 28335–28343 (1999).
- Hoch, R. V. & Soriano, P. Roles of PDGF in animal development. *Development* **130**, 4769–4784 (2003).
- Tallquist, M. D. & Soriano, P. Cell autonomous requirement for PDGFR α in populations of cranial and cardiac neural crest cells. *Development* **130**, 507–518 (2003).
- Morikawa, S. et al. Prospective identification, isolation, and systemic transplantation of multipotent mesenchymal stem cells in murine bone marrow. *J. Exp. Med.* **206**, 2483–2496 (2009).
- Pinho, S. et al. PDGFR α and CD51 mark human Nestin⁺ sphere-forming mesenchymal stem cells capable of hematopoietic progenitor cell expansion. *J. Exp. Med.* **210**, 1351–67 (2013).
- Naganathan, S. R. & Oates, A. C. Patterning and mechanics of somite boundaries in zebrafish embryos. *Semin. Cell Dev. Biol.* **107**, 170–178 (2020).

35. Lee, R. T. H., Knapik, E. W., Thiery, J. P. & Carney, T. J. An exclusively mesodermal origin of fin mesenchyme demonstrates that zebrafish trunk neural crest does not generate ectomesenchyme. *Development* **140**, 2923–2932 (2013).
36. Helker, C. S. M. et al. The zebrafish common cardinal veins develop by a novel mechanism: lumen ensheathment. *Dev* **140**, 2776–2786 (2013).
37. Van Kempen, L. C. L. T. et al. Molecular basis for the homophilic activated leukocyte cell adhesion molecule (ALCAM)-ALCAM interaction. *J. Biol. Chem.* **276**, 25783–25790 (2001).
38. Singh, J., Sharma, K. & Pillai, P. P. PDGFR inhibition mediated intracellular signalling in C6 glioma growth and migration: role of ERK and ROCK pathway. *Cytotechnology* **70**, 465–477 (2018).
39. Ip, C. K. M. et al. Neomorphic PDGFRA extracellular domain driver mutations are resistant to PDGFRA targeted therapies. *Nat. Commun.* **9**, 4583 (2018).
40. French, C. et al. Mutation of FOXC1 and PITX2 induces cerebral small-vessel disease. *CLIN J.* **124**, 4877–4881 (2014).
41. Fruman, D. A. et al. The PI3K pathway in human disease. *Cell* vol. **170**, 605–635 (2017).
42. Pouget, C. et al. FGF signalling restricts haematopoietic stem cell specification via modulation of the BMP pathway. *Nat. Commun.* **5**, 5588 (2014).
43. Cattaneo, P. et al. Parallel lineage-tracing studies establish fibroblasts as the prevailing in vivo adipocyte progenitor. *Cell Rep.* **30**, 571–582 (2020).
44. Ando, K., Shibata, E., Hans, S., Brand, M. & Kawakami, A. Osteoblast production by reserved progenitor cells in zebrafish bone regeneration and maintenance. *Dev. Cell* **43**, 643–650.e3 (2017).
45. Caplan, A. I. Mesenchymal stem cells: time to change the name! *Stem Cells Transl. Med.* **6**, 1445–1451 (2017).
46. Khan, J. A. et al. Fetal liver hematopoietic stem cell niches associate with portal vessels. *Science* **351**, 176–180 (2016).
47. Caplan, A. I. & Bruder, S. P. Mesenchymal stem cells: building blocks for molecular medicine in the 21st century. *Trends Mol. Med.* vol. **7**, 259–264 (2001).
48. Nguyen, P. D. et al. Haematopoietic stem cell induction by somite-derived endothelial cells controlled by meox1. *Nature* **512**, 314–318 (2014).
49. Kobayashi, I. et al. Jam1a-Jam2a interactions regulate haematopoietic stem cell fate through Notch signalling. *Nature* **512**, 319–323 (2014).
50. Clements, W. K. & Traver, D. Signalling pathways that control vertebrate haematopoietic stem cell specification. *Nat. Rev. Immunol.* **13**, 336–348 (2013).
51. Naganathan, S. R., Popović, M. & Oates, A. C. Left-right symmetry of zebrafish embryos requires somite surface tension. *Nature* **605**, 516–521 (2022).
52. Nelissen, J. M. D. T., Peters, I. M., De Groot, B. G., Van Kooyk, Y. & Figdor, C. G. Dynamic regulation of activated leukocyte cell adhesion molecule-mediated homotypic cell adhesion through the actin cytoskeleton. *Mol. Biol. Cell* **11**, 2057–2068 (2000).
53. Kimmel, C. B., Ballard, W. W., Kimmel, S. R., Ullmann, B. & Schilling, T. F. Stages of embryonic development of the zebrafish. *Dev. Dyn.* **203**, 253–310 (1995).
54. Parinov, S., Kondrichin, I., Korzh, V. & Emelyanov, A. Tol2 transposon-mediated enhancer trap to identify developmentally regulated zebrafish genes in vivo. *Dev. Dyn.* **231**, 449–459 (2004).
55. Seger, C. et al. Analysis of Pax7 expressing myogenic cells in zebrafish muscle development, injury, and models of disease. *Dev. Dyn.* **240**, 2440–2451 (2011).
56. Moro, E. et al. In vivo Wnt signaling tracing through a transgenic biosensor fish reveals novel activity domains. *Dev. Biol.* **366**, 327–340 (2012).
57. Chi, N. C. et al. Foxn4 directly regulates tbx2b expression and atrioventricular canal formation. *Genes Dev.* **22**, 734–739 (2008).
58. Zhu, H. et al. Regulation of the lmo2 promoter during hematopoietic and vascular development in zebrafish. *Dev. Biol.* **281**, 256–269 (2005).
59. Suster, M. L., Abe, G., Schouw, A. & Kawakami, K. Transposon-mediated BAC transgenesis in zebrafish. *Nat. Protoc.* **6**, 1998–2021 (2011).
60. Bussmann, J. & Schulte-Merker, S. Rapid BAC selection for tol2-mediated transgenesis in zebrafish. *Development* **138**, 4327–4332 (2011).
61. Le Guyader et al. Origins and unconventional behavior of neutrophils in developing zebrafish. *Blood* **111**, 132–141 (2008).
62. Swartz, M. E., Sheehan-Rooney, K., Dixon, M. J. & Eberhart, J. K. Examination of a palatogenic gene program in zebrafish. *Dev. Dyn.* **240**, 2204–2220 (2011).
63. Charbord, P. et al. A systems biology approach for defining the molecular framework of the hematopoietic stem cell niche. *Cell Stem Cell* **15**, 376–391 (2014).
64. Bickers, C., Española, S. D., Grainger, S., Pouget, C. & Traver, D. Zebrafish snai2 mutants fail to phenocopy morphant phenotypes. *PLoS ONE* **13**, e0202747 (2018).
65. Das, A. & Crump, J. G. Brms and Id2a act upstream of Twist1 to restrict ectomesenchyme potential of the cranial neural crest. *PLoS Genet.* **8**, e1002710 (2012).
66. Herbomel, P. & Levrard, J. P. Imaging early macrophage differentiation, migration, and behaviors in live zebrafish embryos. *Methods Mol. Med.* **105**, 199–214 (2005).
67. Schindelin, J. et al. Fiji: an open-source platform for biological-image analysis. *Nat. Methods* **9**, 676–682 (2012).
68. Zengel, P. et al. μ -Slide chemotaxis: a new chamber for long-term chemotaxis studies. *BMC Cell Biol.* **12**, 21 (2011).
69. Urbancic, V. et al. Filopodyan: an open-source pipeline for the analysis of filopodia. *J. Cell Biol.* **216**, 3405–3422 (2017).

Acknowledgements

We thank our fish facility team for zebrafish care, K. Kawakami (National Institute of Genetics, Mishima) for providing us with the BAC recombining plasmids, T.J. Carney (IMCB, Singapore) for Tg(ola-twist:Gal4; UAS:Kaede) fish, R. Patient (University of Oxford) for the hsp70-4:pG1 plasmid, J. Eberhart (University of Texas at Austin) for the pdgfra:pCR4 plasmid, B. Appel (University of Colorado) for the cspg4:pJC53.2 plasmid, and A. Kudo (Tokyo Institute of Technology, Nagatsuta) for the pax9:pPACT3 plasmid. We also thank S. Rigaud, D. Ershov, and J.-Y. Tinevez (IAH of Institut Pasteur) for the implementation of Python scripts for filopodia analysis. We thank L. Tchou (Fondation de l'AP-HP) for working with us on our initial trials on the pax9 project. We thank A.-L. Touret (Institut Pasteur) for her contribution to setting up the Western blot experiments, and K. McElreavey, D. Houzelstein, and C. Eozenou (Institut Pasteur) for their help with Luciferase assays. This work was supported by Institut Pasteur, CNRS, and by grants to P.H. from the Fondation pour la Recherche Médicale (#DEQ20160334881), the Fondation ARC pour la Recherche sur le Cancer, and the Agence Nationale de la Recherche Laboratoire d'Excellence Revive (Investissement d'Avenir; ANR-10-LABX-73).

Author contributions

E.M. conceived the project, designed, performed, and analyzed experiments, and wrote the paper. C.V. conducted experiments and fish care. A.S. conducted experiments and assisted with helpful discussions. P.H. ensured the funding of the project, analyzed, discussed, and suggested experiments, and wrote the paper.

Competing interests

The authors declare no competing interests.

Additional information

Supplementary information The online version contains supplementary material available at <https://doi.org/10.1038/s41467-023-36612-y>.

Correspondence and requests for materials should be addressed to Emi Murayama.

Peer review information *Nature Communications* thanks Leonard Zon and the other, anonymous, reviewer(s) for their contribution to the peer review of this work. Peer reviewer reports are available.

Reprints and permissions information is available at <http://www.nature.com/reprints>

Publisher's note Springer Nature remains neutral with regard to jurisdictional claims in published maps and institutional affiliations.

Open Access This article is licensed under a Creative Commons Attribution 4.0 International License, which permits use, sharing, adaptation, distribution and reproduction in any medium or format, as long as you give appropriate credit to the original author(s) and the source, provide a link to the Creative Commons license, and indicate if changes were made. The images or other third party material in this article are included in the article's Creative Commons license, unless indicated otherwise in a credit line to the material. If material is not included in the article's Creative Commons license and your intended use is not permitted by statutory regulation or exceeds the permitted use, you will need to obtain permission directly from the copyright holder. To view a copy of this license, visit <http://creativecommons.org/licenses/by/4.0/>.

© The Author(s) 2023